THE PRE-CME SUN

Report of Working Group E

N. GOPALSWAMY[1], Z. MIKIĆ[2], D. MAIA[3], D. ALEXANDER[4], H. CREMADES[5], P. KAUFMANN[6], D. TRIPATHI[5] and Y.-M. WANG[7]
[1]*NASA Goddard Space Flight Center, Greenbelt, Maryland, USA*
[2]*SAIC, 10260 Campus Point Drive, San Diego, CA 92121-1578 USA*
[3]*CICGE, Faculdade Ciências Universidade Porto, Portugal*
[4]*Department of Physics and Astronomy, Rice University, 6100 Main St, Houston, TX 77005, USA*
[5]*Max-Planck-Institute for Solar System Research, 37191 Katlenburg-Lindau, Germany*
[6]*CRAAM, Mackenzie Presbyterian University, S. Paulo, Brazil*
[7]*Naval Research Laboratory, Washington, DC, USA*
*(*Author for correspondence: E-mail: gopals@ssedmail.gsfc.nasa.gov)*

(Received 3 February 2006; Accepted in final form 12 June 2006)

Abstract. The coronal mass ejection (CME) phenomenon occurs in closed magnetic field regions on the Sun such as active regions, filament regions, transequatorial interconnection regions, and complexes involving a combination of these. This chapter describes the current knowledge on these closed field structures and how they lead to CMEs. After describing the specific magnetic structures observed in the CME source region, we compare the substructures of CMEs to what is observed before eruption. Evolution of the closed magnetic structures in response to various photospheric motions over different time scales (convection, differential rotation, meridional circulation) somehow leads to the eruption. We describe this pre-eruption evolution and attempt to link them to the observed features of CMEs. Small-scale energetic signatures in the form of electron acceleration (signified by nonthermal radio bursts at metric wavelengths) and plasma heating (observed as compact soft X-ray brightening) may be indicative of impending CMEs. We survey these pre-eruptive energy releases using observations taken before and during the eruption of several CMEs. Finally, we discuss how the observations can be converted into useful inputs to numerical models that can describe the CME initiation.

Keywords: coronal mass ejections, flares, radio bursts, filaments, prominences, streamers, solar magnetism, active regions, closed and open magnetic fields, pre-eruption signatures, energy storage and release, helicity

1. Introduction to the Pre-CME Sun

Understanding the pre-eruption state of the solar sources of CMEs is a key aspect in unraveling the mystery behind CME initiation. There is also an important practical application: if it is possible to identify some parameter that may indicate a high probability for eruption, then one should be able to predict the imminent occurrence of a CME and hence the accompanying interplanetary consequences. In order to understand the pre-eruption state, we need to consider three aspects of an eruption region on the Sun: (i) the magnetic structure, (ii) the evolution, and (iii) the energetic

Space Science Reviews (2006) 123: 303–339
DOI: 10.1007/s11214-006-9020-2

signatures. The very basic requirement in an eruption region is that it contains closed magnetic field structure identified in longitudinal magnetograms by pairs of positive and negative magnetic polarity patches. A simple closed field structure may not have enough free energy to be ejected as a CME, so the closed field structure has to be distorted by pre-eruption evolution that adds free energy, generally referred to as energy build-up. Shearing motions, flux emergence and cancellation, and sunspot rotations in the source region are some of the processes that occur in the energy build-up phase and can result in small-scale energy releases distinct from the eruption itself. Such small-scale heating and non-thermal radio emission (indicative of particle acceleration) are considered to be signatures of the energy build-up and release.

It must be noted that extensive literature exists on preflare activities (see e.g. Priest *et al*., 1986; Simnett, 1999). While not all flares are associated with CMEs, the precursor activity in eruptive flares is expected to be similar to that for CMEs. All the aspects of the structure, evolution and energetics of the preflare source region are applicable to the pre-CME source region.

The free magnetic energy is typically found to be twice the potential energy of the eruption region (Mackay *et al*., 1997; Forbes, 2000; Metcalf *et al*., 1995), although recent results indicate the possibility of much higher factors (Metcalf *et al*., 2004). In this chapter we focus on the energy build-up and describe the three basic aspects of eruption regions.

After an introduction to the pre-CME Sun (Section 1), the pre-eruption structure (Section 2), pre-eruption evolution (Section 3), and pre-eruption energetic signatures (Section 4) are presented. Global issues related to the pre-CME Sun are discussed in Section 5. The final Section 6 contains discussion and summary with a brief note on future perspectives.

2. Pre-Eruption Structure

The characteristics and dynamics of CMEs are inherently related to the properties and behavior of their associated near-surface features. Consequently, what we observe in a CME source region prior to the eruption may yield important insight into the eruption process itself. Quiescent features in the various layers of the solar atmosphere need to be pieced together to fully understand the pre-eruption structure of a CME. The type of magnetic field configurations we infer from observations and how they relate to the observed structure of CMEs is presented in this section.

2.1. Closed and Open Field Regions on the Sun

The basic magnetic structure of the solar atmosphere consists of open and closed field. The closed field regions are typically comprised of active regions, quiescent filament regions, and transequatorial interconnecting regions. Filaments

are regarded as one of the fundamental solar sub-structures relevant to coronal mass ejections: solar source regions occasionally include both filaments and active regions, with the filaments lying outside, but close to the active regions. The primary difference between the filament regions and active regions is simply characterized by the strength and structure of the magnetic field involved. Active regions typically have much higher field strength in a compact volume, while filament regions have lower field strength, typically elongated along the filament axis (although there are exceptions). The post-eruption structures are also accordingly different in the two cases. Transequatorial structures generally appear during solar minimum, when the active regions are much closer to the equator. An eruption involving a transequatorial region occurs over a larger volume than one involving a single active region.

Figure 1 shows the Sun during October 17–18, 1999 at four different wavelengths, corresponding to four different heights in the atmosphere: a longitudinal

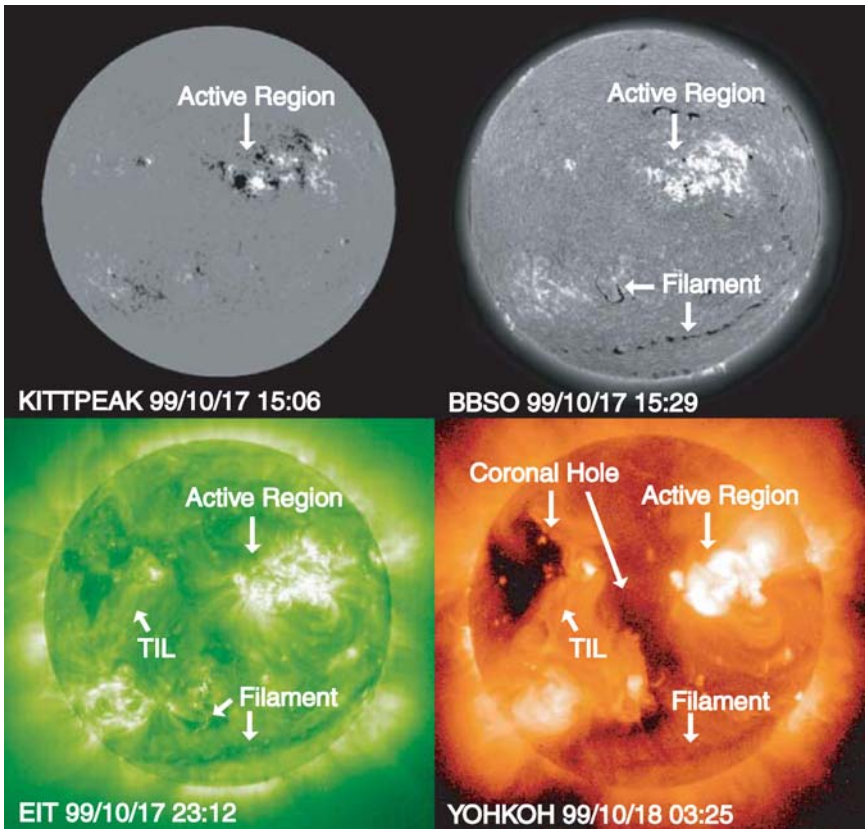

Figure 1. Large-scale solar magnetic regions such as active regions and filament regions that have closed field structure (CME-producing regions) and coronal holes with open field structure that do not produce CMEs. TIL–transequatorial interconnecting region.

magnetogram from SOHO/MDI, an Hα picture from the Big Bear Solar Observatory, an EUV image at 195 Å from SOHO/EIT, and a soft X-ray image from Yohkoh. The active region complex contains five numbered regions, the largest one being AR 8731. The active region complex appears brightest in all images. The active region loops are hotter and denser and hence have bright coronal emission. The elongated dark features are the filaments, which delineate opposite polarity patches both in the active region and in the quiet regions. As the active region developed, the U-shaped filament in the Hα image erupted, as captured in the SOHO/EIT image: the filament appears bright in EUV probably because it was heated during eruption. A prominent transequatorial structure can be seen in the SXT and in EIT images (marked TIL), connecting AR 8735 in the north (N18E22) and AR 8736 (S20E35) in the south. In principle, all of these closed field structures could erupt provided they have enough free energy. One can also see coronal holes, which appear as dark patches in the SXT and EIT images. The magnetic field inside the largest coronal hole in the northwest quadrant is enhanced and of unipolar (positive) polarity. While fast solar wind originates from such coronal holes, CMEs do not.

White-light observations of CMEs show a wealth of different morphologies, ranging from amorphous blobs, to simple narrow jet-like features, up to highly structured and complicated entities. While CMEs exclusively originate from closed magnetic field regions, there are situations in which there is an interaction between closed and open field regions. We shall first consider the structure of CMEs that originate from closed field regions and then briefly discuss narrow CMEs resulting from the interaction between closed and open field structures.

2.2. Three-Part Structure

Many white-light CMEs display a characteristic three-part structure: a bright leading edge, a dark void (cavity) and a bright core (Illing and Hundhausen, 1985). Figure 2 shows an example of a three-part CME recorded by SOHO/LASCO. The frontal structure is coronal material, the cavity also is coronal, but may have higher magnetic fields and lower density, and the bright core is the eruptive prominence. The three-part structure is seen in only about 30% of CMEs, yet this is viewed as the "standard CME" configuration in observational and theoretical studies. The circular pattern observed within the cavities of many CMEs suggests the existence of helical magnetic features (Chen *et al*., 1997; Dere *et al*., 1999; Wood *et al*., 1999), commonly known as flux ropes and used extensively by CME modelers. *In-situ* measurements of magnetic clouds linked to filament eruptions (Marubashi, 1986; Gopalswamy *et al*., 1998), and the discovery of filament material inside the magnetic cloud (Burlaga *et al*., 1998) support this association.

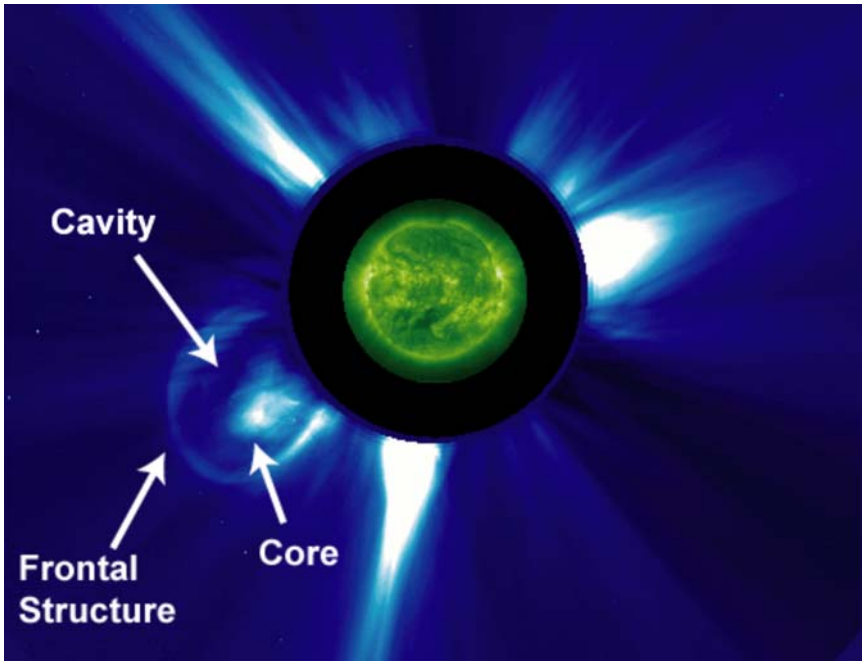

Figure 2. SOHO/LASCO image (with an EIT 195 image superposed) obtained on 2001 December 20 showing the three-part structure of a CME above the southwest limb.

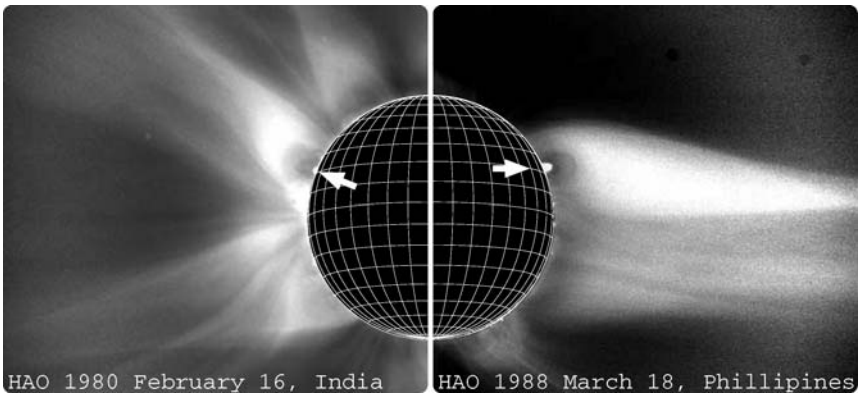

Figure 3. White-light eclipse images showing bright streamers overlying cavities with filaments inside (indicated by the arrows). Courtesy High Altitude Observatory.

The three-part structure is commonly observed in eclipse pictures (Saito and Tandberg-Hanssen, 1973). Figure 3 shows two eclipse images where the three-part structure is clearly evident. The subsequent eruption of this structure then becomes the three-part CME. The prominence and cavity become the bright core and flux rope of the CME, while the streamer deforms to become the frontal structure. The direct

connection between pre-eruption and CME components can be shown by means of height-time plots, which reveal the continuity of the three different CME parts when the fields of view of different instruments overlap (Illing and Hundhausen, 1985; Srivastava *et al*., 1999; Plunkett *et al*., 2000; Gopalswamy *et al*., 2003b).

2.2.1. *The Bright Core*

The bright core is the feature of CMEs whose near-surface counterpart is best known. The white-light core of CMEs has been shown to be the eruptive filament observed in Hα (House *et al*., 1981) or in micro-waves (Gopalswamy, 1999) close to the surface. Solar filaments, called "prominences" when viewed above the limb, have an observational heritage significantly older than that of CMEs. Prominence eruptions, discovered in the 1800s, were in fact one of the earliest forms of mass ejection to receive attention (for a historical introduction see Tandberg-Hanssen, 1995). Filaments are lanes of cool (7000 K) plasma embedded in the corona that lie, without exception, above the photospheric magnetic neutral lines (Babcock and Babcock, 1955). They are located within the so-called filament channels, where the orientation of chromospheric fibrils along the filament axis suggests a strongly sheared magnetic field (Martin, 1998a). Filaments have traditionally been observed in the Hα line, but are also visible in the EUV or soft X-rays as dark structures (Vaiana *et al*., 1973). Prominences are optically thick in microwaves, so they appear as dark elongated features on the disk and bright features above the limb as in Hα (Gopalswamy, 1999). In fact prominences are the brightest features outside the solar disk in microwaves. Figure 4 shows a prominence seen in different wavelengths.

Although bright cores are commonly observed in CMEs, their presence is not necessary: many structured CMEs are not three-part but two-part, being composed only of a bright leading edge and a cavity. Even for those CMEs associated with

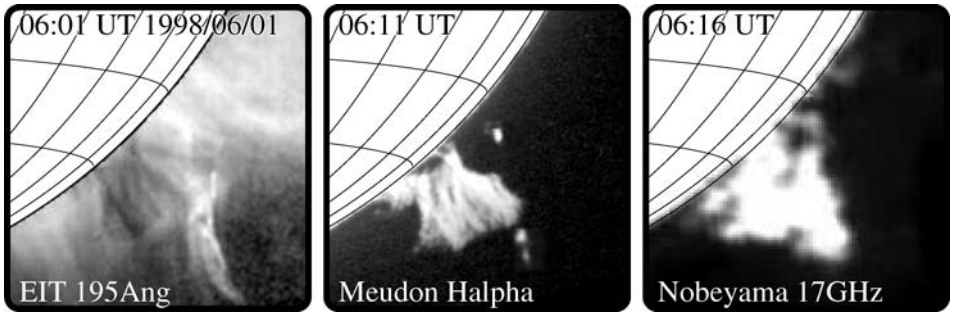

Figure 4. Prominence seen in different wavelengths. (left) The quiescent prominence is seen in EUV as a series of dark features, each looking like an inverted "Y". The bright (middle) prominence seen in Hα in emission. Note the good correspondence between each of the features seen in EUV and Hα. (right) In microwaves the prominence is seen in emission, and there is good correspondence with other wavelengths.

prominence eruptions, only 60% to 70% show a bright core (Hori and Culhane, 2002; Gopalswamy *et al*., 2003b). Not all filaments that erupt lead to CMEs, and there are some strikingly different results on the fraction of prominence eruptions that lead to CMEs. Early work by Webb *et al*. (1976) found that all filament disappearances they examined had a "transient coronal manifestation". This result was confirmed in more recent work by Gilbert *et al*. (2000), Hori and Culhane (2002), and Gopalswamy *et al*. (2003b), with association rates that varied between 70% to 90%. On the other hand, Yang and Wang (2002) have found that, in a total of 431 prominence eruptions, only 10% to 30% were associated with CMEs. The discrepancy may be due in part to selection criteria, mainly in the maximum height attained by the prominence. In fact, Munro *et al*. (1979) observed that while all prominence eruptions seen beyond $1.2R_{\odot}$ were associated with CMEs, only about 60% of those seen beyond 1.1 but below $1.2R_{\odot}$ were associated with CMEs. They noted also that about two thirds of reported eruptive prominences are in fact not seen above $1.1R_{\odot}$; and these show a rate of association with CMEs of only about 10%. The relation between prominence height and CME association has recently been confirmed using the height-time history of eruptive prominences and their associated CMEs (Gopalswamy *et al*., 2003b).

2.2.2. *The Cavity*

The cavity is a localized lack of emission (see Figure 3), in white-light images. Engvold (1988) found this brightness depression to be due to a drop of 50% to 75% in the local electron density in the immediate vicinity of the filament and the overlying coronal arcades. It is tempting to see this cavity as the outer part of the magnetic structure (flux rope) sustaining the filament (Low and Hundhausen, 1995), but other possibilities have been proposed. Martin (1998a) defines the cavity as the volume between features of opposite chirality. The void exists because structures with opposite chirality cannot conjoin.

Cavities are also seen in EUV and soft X-ray images (Vaiana *et al*., 1973; Hudson *et al*., 1999). An example, observed by EIT in 195Å, on 1997 December 3, is shown in Figure 5. On this day three filament channels were seen extending close to the limb, with dark thin filaments clearly visible inside each of them. Overlying each of these filaments a cavity is seen reaching an altitude about $0.15R_{\odot}$ over the solar limb.

EUV and X-ray observations show cavities only at the limb. At radio wavelengths, cavities can be observed on the disk as brightness depressions (Kundu and McCullough, 1972; Gopalswamy *et al*., 1991; Marqué, 2004). The brightness depressions at 20 cm wavelength were found to have a larger extent than the filament itself at higher temperature (Gopalswamy *et al*., 1991). Decimetric radio images from the Nançay Radioheliograph show cavities overlying filaments observed in Hα. The observed radio depression in the a cavity implies a density drop of 25% to 50% from the mean coronal density (75% for one event). The radio cavities match the extent of filament channels, and are continuous features even when the associated Hα filament is not. When seen erupting, the radio depression overlies

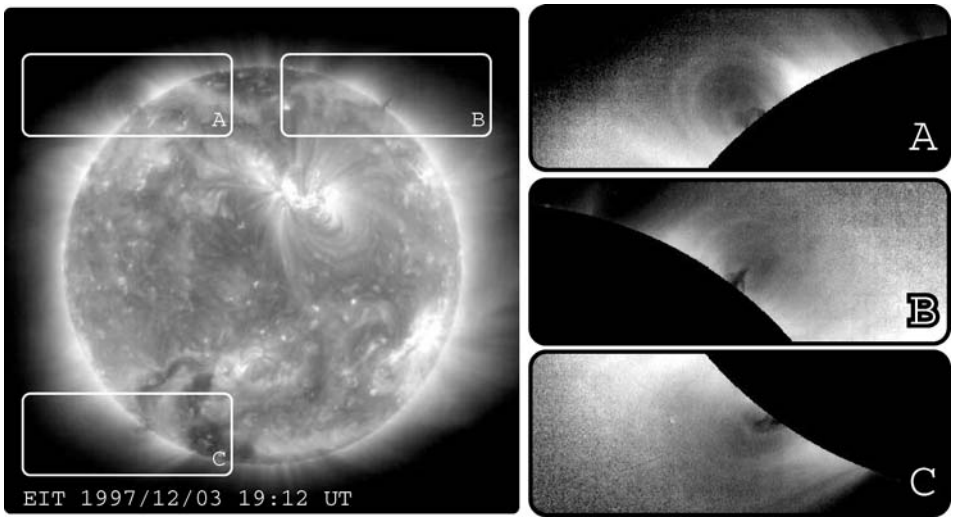

Figure 5. Cavities overlying EUV filaments as seen by EIT on 1997 December 3, in 195 Å bandpass.

the erupting filament (Marqué *et al*., 2002), suggesting that the radio depression is linked to the filament, in agreement with flux-rope models of filaments (Low and Hundhausen, 1995).

2.2.3. *The Frontal Structure*

The frontal structure of CMEs (the bright leading edge) represents density enhancements from 10 to 100 times the background corona (below $6R_{\odot}$). The average mass of CMEs is about 2×10^{15} g, with a significant fraction of CMEs (15%) having masses below 10^{14} g (Vourlidas *et al*., 2002). The question is where does all that mass come from and what kind of features in the low corona account for the frontal structure? It has been suggested that the mass in the overlying pre-eruptive arcade could account for most of the mass in CMEs (Hudson *et al.*, 1996; Gopalswamy and Hanaoka, 1998). Some observations indicate that prominences also carry approximately the same mass as the frontal structure (Gopalswamy and Hanaoka, 1998). As the CME proceeds into the corona, it will likely sweep up additional material so that the mass would increase, at least in the beginning. As the CME moves out, the frontal structure near the Sun is likely to evolve into the sheath material behind interplanetary shocks observed *in situ* (Gopalswamy, 2003). Transequatorial loop systems (TLS) have masses around 10^{15} g (Khan and Hudson, 2000). These may become part of the larger CMEs (Delannée and Aulanier, 1999; Wills-Davey and Thompson, 1999; Khan and Hudson, 2000) and as such can account for a substantial fraction of the CME mass. Glover *et al*. (2003) have found that TLS are likely to contribute mass to a CME if at least one of the following happens: (1) two active regions are involved, (2) the TLS is extended, (3) the longitudinal asymmetry is

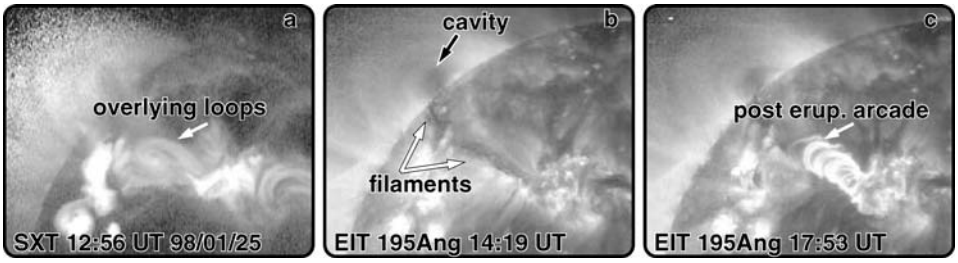

Figure 6. Pre-event versus post-event configuration of a CME source region. (a) and (b) The pre-event shows a system of sheared loops overlying a filament. (c) After the CME lift-off magnetic restructuring gives rise to an arcade of loops perpendicular to the neutral line.

high. Unfortunately no comprehensive study of TLS association with CMEs has been made to date.

2.2.4. *Relation to Post-Eruption Arcade*

Post-eruptive arcades (PEAs) are defined as the formation of transient large-scale loop systems straddling the neutral line, following an eruption. Figure 6 shows an example of such a feature. The PEAs are typically observed over a time period of several hours on the solar disk in EUV and X-rays (Webb *et al*., 1978; Zarro *et al*., 1999; Sterling *et al*., 2000; Gopalswamy, 2003; Tripathi *et al*., 2004). In Hα, they are referred to as post-flare loops. Occasionally, the PEAs are observed in microwaves as enhanced thermal free-free emission (Hanaoka *et al*., 1994). The foot points of a series of PEA loops form the ribbons visible in Hα (the two-ribbon flares). EUV PEAs observed by SOHO/EIT (195 Å) from 1997 to 2002 had an average duration of $\sim$7 hours and an average length of $\sim$15 degrees (Tripathi *et al*., 2004). Kopp and Pneuman (1976) have interpreted the formation of loop systems as a consequence of magnetic reconnection in the aftermath of the CME eruption. One of the interesting questions is how these PEAs evolve to become the frontal structures of future CMEs.

2.3. Filament Eruption Near Coronal Holes

Filaments located in the vicinity of coronal holes have shown some proclivity for eruption. This was first pointed out by Webb *et al*. (1978) using Hα and Skylab X-ray data. Webb *et al*. (1978) studied the relation between X-ray PEAs and the long and short-term variability in coronal hole boundaries and found that they occurred over neutral lines which form the borders of evolving coronal holes. The associated filaments were observed to rotate rigidly (compared to the photospheric plasma) similar to the coronal holes (Adams, 1976). A similar study was conducted using Yohkoh data by Bhatnagar (1996). Webb *et al*. (1976) also found that the eruptions are associated with coronal holes growing in area while Bravo (1996) suggested that

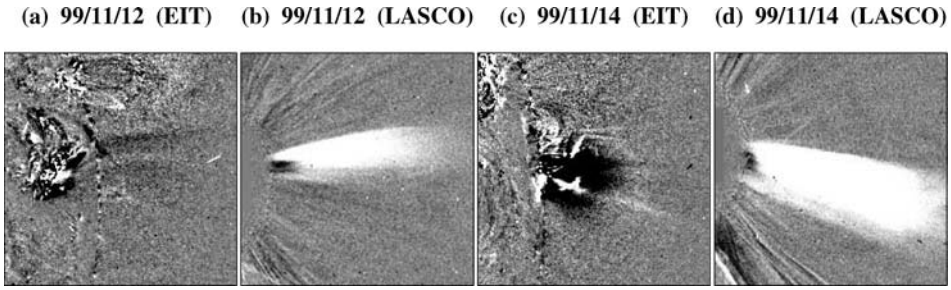

Figure 7. Narrow, jet-like CMEs originating from an active region inside a coronal hole, 1999 November 12 and 14. (a) and (c) show the two events as observed near the solar surface with EIT (each panel represents the difference between two Fe XII λ195 images taken 12 min apart). (b) and (d) show the same events as observed above $r \sim 2R_{\odot}$ over the west limb with the LASCO C2 coronagraph. Both CMEs had velocities of the order of 1000 km/s.

the coronal hole area may increase due to the eruption of nearby filaments. Thus the location of filaments near coronal holes can be considered as a pre-eruption state with a propensity for eruption. These studies need to be repeated with the uniform and extensive data set available from SOHO. For example, SOHO/EIT data can provide information on coronal holes and filaments. Filament eruptions are readily observed in the EUV images and can be compared with SOHO/LASCO data for the associated CMEs. Eruptions of filaments not located close to coronal holes can be used as a control sample.

2.4. Jets, Narrow CMEs, and Their Relation to Coronal Holes

There is a particular class of mass ejection that appears to be triggered by the interaction between closed and open magnetic fields and that is closely associated with coronal holes. During the 1996–1997 activity minimum, the LASCO C2 coronagraph detected faint linear structures propagating outward at high speeds from the Sun's polar regions. These white-light jets, which occurred at an average rate of 3–4 per day and which were also seen in O VI and Lyα with UVCS (Dobrzycka *et al.*, 2002), had angular widths of $1^{\circ} - 4^{\circ}$ and leading-edge velocities of ∼400–1100 km/s. They were shown to be the outward extensions of EIT jets that originated from flaring EUV bright points inside the polar coronal holes (Wang *et al.*, 1998). During the 1999–2001 activity maximum, both white-light jets and narrow CMEs having widths $\lesssim 15^{\circ}$ and velocities of up to 1000 km/s were observed to originate from active regions located inside or along the boundaries of low-latitude coronal holes (Wang and Sheeley, 2002). A single active region often gave rise to a succession of such ejections over its lifetime, which were detected by LASCO as the coronal hole rotated past the solar limb (see Figure 7). The basic mechanism underlying all of these jet-like events is presumed to be "interchange" magnetic reconnection between the bipole and coronal hole fields, whereby material

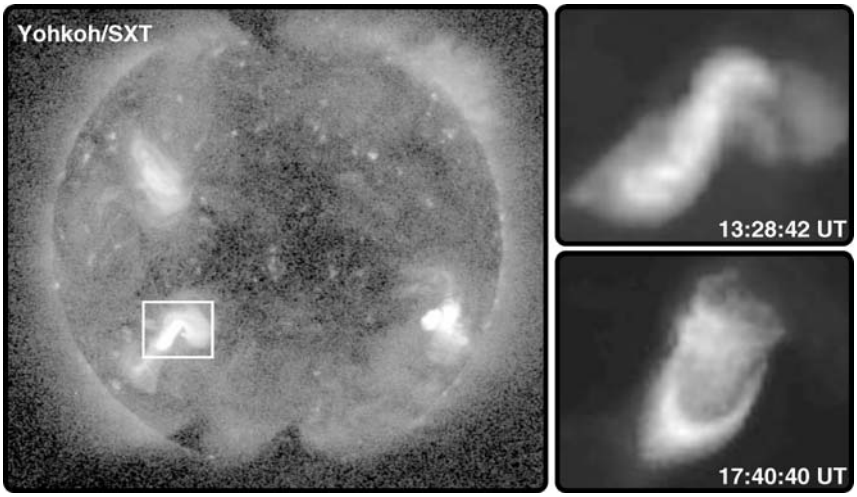

Figure 8. Soft X-ray sigmoid observed by the Yohkoh/SXT. This region erupted with an associated CME: the reconfiguration of the coronal structure in the aftermath of the eruption is evident. Courtesy Yohkoh Team.

is transferred from closed to open fields lines to produce a fast, highly collimated ejection.

2.4.1. *Sigmoids*

An observational manifestation of the connection between coronal structure and CME production is the soft X-ray sigmoid (Rust and Kumar, 1996; Pevtsov and Canfield, 1999; Canfield *et al*., 2000). An example of a sigmoid that gives rise to an eruption is shown in Figure 8. Active regions exhibiting sinuous-S or reverse-S shapes have been shown to exhibit a greater tendency to erupt (Canfield *et al*., 1999). Leamon *et al*. (2002), further demonstrated that when active region sigmoids do erupt, they tend to produce at least moderate geomagnetic storms. Relating the sigmoids at X-ray (and other) wavelengths to magnetic structures and current systems in the solar atmosphere is the key to understanding their relationship to CMEs. The sigmoidal shape suggests that the twist in the magnetic structure may have something to do with the eruption. For instance, the stability of a flux tube seems to be related to the amount of twist it contains (e.g. Priest, 1984; Rust and Kumar, 1994b) with the result that a flux tube becomes unstable above a critical twist of order 2π. However, Leamon *et al*. (2003) have argued that the observed sigmoids fall well short of this critical twist, albeit using an approach which measures an active-region averaged value for the force-free parameter, α, as a measure of the twist in the sigmoid.

The transition from a sigmoid to an arcade in the X-ray observations during the initiation of a CME is strongly suggestive that an instability, and associated topological reconfiguration, has occurred. However, sigmoids may also disappear

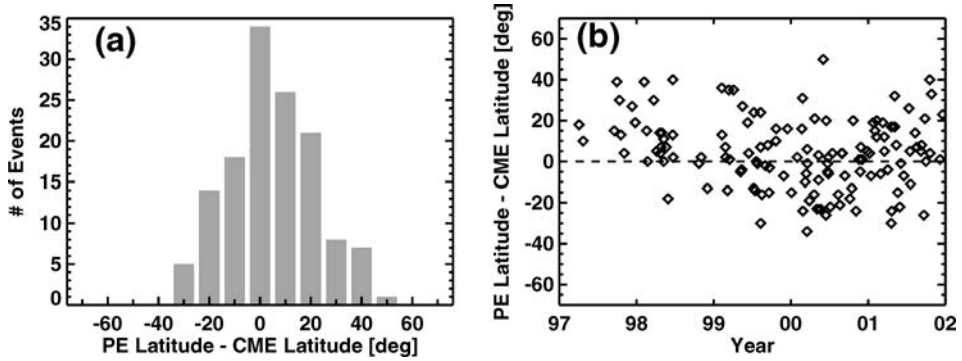

Figure 9. The latitude difference between CMEs and prominence eruptions (PEs) for the period 1996–2001: (a) the distribution of the latitude difference, (b) the latitude difference as a function of time. The reason for the positive offset of PEs in (a) is obvious in (b) because the offset is positive during solar minimum. Towards and during solar maximum, there is no net offset. During solar minimum the dipole field of the Sun is strong and guides the CMEs towards the equator. During the rising phase and maximum the dipole field is considerably weakened and hence the PEs and CMEs have roughly the same position angle. Adapted from Gopalswamy *et al.* (2003b).

and reappear without a detectable CME (see Gibson *et al.*, 2002). We need to understand more about the formation and evolution of sigmoid structures in active regions and to explore the conditions that drive them to eruption. Key components would be the role played by magnetic helicity and how this helicity reaches the corona, via photospheric motions (shearing) or direct emergence of twisted flux.

2.5. Guiding Streamers

During solar minimum, the CME latitude shows a single broad peak centered on the equator, while the source region latitude exhibits a two-peak behavior, with maxima at around $\pm 30^\circ$ (Plunkett *et al.*, 2002; Gopalswamy *et al.*, 2003b; Cremades and Bothmer, 2004). This effect is clearly evident in Figure 9, showing the distribution of the offset between the latitudes of prominence eruptions (PEs) and CMEs (derived from the central position angles). The offset is clearly positive during solar minimum years (the PE latitude is poleward of the CME latitude). The reason for this offset can be explained by the strong influence of the large-scale global solar magnetic field on the erupting structure, as evidenced by the nonradial motion of prominences (Gopalswamy *et al.*, 2000; Filippov *et al.*, 2001). The typical scenario is that the prominence originates from the active region belt, and is channeled into the streamer centered at the heliospheric current sheet, typical of minimum solar activity. Since the majority of the CMEs observed in the field of view of SOHO/LASCO C2, maintain their direction of propagation, the deflection must have already taken place at lower altitudes, i.e. below 2 solar radii. The marked trend in CME position angle toward the equator is not seen at solar maximum: CMEs get deflected in all

directions, reflecting the varied influence of the solar dipolar field on CMEs during solar minimum and maximum.

3. Pre-Eruption Evolution

Pre-eruption evolution can be loosely defined as the process by which closed field structures on the Sun are energized (or become non-potential). One of the simplest ways in which this can happen is by the deformation of the closed field lines as a result of the change in footpoint separation or twisting of one or both footpoints. The deformation resulting from the footpoint translations is referred to as magnetic shear and statistically, regions with sheared magnetic field lines are prone to eruption. Vector magnetograms provide direct evidence for sheared magnetic fields near the photospheric neutral lines (e.g. Krall *et al.*, 1982; Heyvaerts and Hagyard, 1991) and rotation of sunspots causing magnetic shear is often observed. Measurement of shear in active regions is possible from vector magnetograms, and hence provides a simple means of predicting the possibility of large eruptions. Theoretically, as the shear reaches a critical value, the system goes out of equilibrium and the sheared structure erupts (Hagyard *et al.*, 1984). Other processes such as flux emergence and vertical flows may also trigger the eruption of sheared structures (Ambastha, 1998). Flux emergence has long been associated with filament eruption (Canfield *et al.*, 1974), a good indicator of CMEs (Gopalswamy, 2003 and references therein). However, flux emergence seems to be ubiquitous in active regions and its utility as a pre-eruption signature requires more study. Filament activation observed for about 10–30 min before eruption provides further insight into the eruption process itself. The filament activation may represent changes in the background magnetic field or the increase in filament current (see, e.g., Kuperus and van Tend, 1981) which may result from changes caused by shear or flux emergence.

3.1. Shear, Differential Rotation

In the solar corona, the magnetic helicity and excess energy must be supplied by the photospheric or sub-photospheric activity. While theoretical studies of helicity injection have concentrated on the emergence of twist and/or writhe in confined flux tubes (e.g. Magara and Longcope, 2001), observationally most of the emphasis has been on the shearing of the footpoints of coronal structures (Canfield and Pevtsov, 1998; Kusano *et al.*, 2002; Moon *et al.*, 2002) with some effort to determine the flux emergence component (Nindos and Zhang, 2002; Kusano *et al.*, 2002).

Recent results have been confusing about the role the two components play in the production of flares and CMEs, through the build-up of helicity in the corona. On the one hand, DeVore (2000) has argued that a significant quantity of magnetic helicity is injected by the action of differential rotation over the lifetime of an

active region; enough to explain the total ejected helicity detected in interplanetary magnetic clouds, often treated as the interplanetary counterparts of CMEs (Gosling *et al*., 1995). This assertion has been contested by Démoulin *et al*. (2002) and Green *et al*. (2002) who argue that the helicity injected by differential rotation is 5 to 50 times smaller than that inferred to be carried away in CMEs, leaving these authors to conclude that the bulk of the helicity injection is provided by the twist in the sub-photospheric part of the magnetic flux tubes forming active regions. Proving this observationally is difficult since the measurement of the helicity injection from flux emergence not only requires vector magnetic field information but also knowledge of the vertical velocity component of the emergence (cf. Kusano *et al*., 2002).

In the debate over the role of differential rotation, the strong local shearing often observed near the magnetic neutral line(s) of flare-productive active regions (e.g Harvey and Harvey, 1976) is frequently neglected. Such strong local shear may contribute significantly to the helicity injection into large but otherwise local structures associated with the active region. Recent studies by Kusano *et al*. (2002), Nindos and Zhang (2002) and Moon *et al*. (2002) have demonstrated that multiple flaring is often associated with regions of strongly sheared footpoint motions and local helicity injection. In the case discussed by Kusano *et al*. (2002) the shearing motions can contribute as much, if not more, helicity as the flux emergence.

3.2. Photospheric Flows

The evolution of the magnetic field is crucial in driving the solar corona to erupt in a CME. Unfortunately, routine observations of the 3D magnetic field can only be performed in the solar photosphere, where the conditions are demonstrably non-force-free (Metcalf *et al*., 1995). The desired coronal field is then obtained using extrapolation techniques with the photospheric observations serving as a boundary condition and assuming, typically, that the field is force-free (e.g. Démoulin *et al*., 1997). More recent approaches, made viable by continuously improving computational resources, adopt fully 3D MHD modeling of the of the coronal magnetic field incorporating the observed field and plasma data at the photospheric boundary (Abbett and Fisher, 2003). These data-driven boundary conditions then require detailed observations of the evolution not only of the magnetic field but also of the plasma, i.e. in order to fully understand the physical processes governing CME initiation we need to understand the role played by plasma flows in the photosphere.

The coupling of the photospheric dynamics and the coronal evolution is, at best, unclear. Evidence of flows associated with eruptive phenomena comes in the form of divergence of magnetic flux as new flux emerges, shearing motions in the photosphere, and the collision of opposite magnetic polarities leading to flux cancellation. Early studies on large flares indicated that shearing motions in the photosphere provided the mechanism by which energy was stored in the corona prior to eruption (e.g. Hagyard *et al*., 1984). However, the relationship between

sheared field and eruptive phenomena has not been conclusive, with some events occurring far from sheared neutral line and some eruptive sites exhibiting increased shear after the event (see review by Wang, 1993). Recently, observations of rotating sunspots have been instrumental in relating photospheric motions to helicity injection and subsequent CME initiation (Brown *et al*., 2003). Numerical simulations generally incorporate photospheric motions in an ad hoc way, although efforts to include observations are progressing (see below). CME initiation models have been developed where the corona is driven to eruption by the emergence of twisted flux from below the surface (e.g. Fan, 2001), by subjecting the footpoints of coronal field to vortical motions (e.g. Roussev *et al*., 2004a), and by including flux cancellation via converging flows (Amari *et al*., 2003a).

Ideally, one would need to categorize all three components of the photospheric velocity. This is very difficult in practice although some progress is being made with a variety of techniques. An older and commonly used method is that of local correlation tracking (LCT: November and Simon, 1988) where displacements of identifiable features observed in the white-light continuum are correlated to determine the bulk transverse plasma flow. The problems with this approach are evident. One must not only be able to identify coherent features in the data but these features must last sufficiently long to be observed in several images: LCT results on SOHO/MDI data can require several hours of continuous data (see Berger *et al*., 1998). In the source regions of flares and CMEs the field is evolving rapidly, with emerging and canceling flux limiting the accuracy of the LCT approach. Welsch *et al*. (2004) modified the standard LCT approach which incorporates the inductive equation to better determine the transverse velocity components. However, the LCT velocity may not be consistent with the induction equation and, consequently, Longcope (2004) has developed a parametric approach to solving the inductive equation independently from the LCT velocity results.

The detailed coupling between the observational data and the theoretical modeling is yielding important new results that will allow us to determine which properties of the field and velocity evolution are critical in driving the corona to eruption.

3.3. Emerging Flux

The connection between emerging flux and the CME can be readily established by comparing magnetograms and filament observations because the filament starts erupting very close to the site of emerging flux. The current paradigm is that the emerging flux leads to reconnection with the pre-existing flux. This means that the orientation of the emerging field lines should be favorable for reconnection. It is well known that flux emergence rate is an order of magnitude higher in active regions than in quiet regions (Liggett and Zirin, 1984). Since flux emergence is ubiquitous, it is not often easy to directly link the flux emergence to filament eruptions. However, in retrospect, it is generally possible to identify magnetic field changes on either side of the neutral line (Lara *et al*., 2000).

Figure 10 shows a case of well-observed flux emergence on 2000 September 12. The flux emerged on the positive polarity side of the photospheric neutral line, with a large overlying filament. The region itself is an extended bipolar region with no sunspots (AR 9163 located at S17W09). The positive polarity of the emerging flux is not seen distinctly because it emerges into the existing positive polarity. The negative polarity region appears as a tiny circular region around 06:23 UT, rapidly spreading to become an elongated region by 11:15 UT. The filament, visible in the EIT 195 Å images, showed signs of activation coincident with the flux emergence, displayed rapid motion along the axis and then lifted off by 11:15 UT. The filament eruption was followed by an M1.0 flare starting at 11:32 UT. The associated CME first appeared above the limb at 11:54 UT. The CME had a relatively large acceleration (58.2 m/s^2), typical of CMEs associated with filament eruption. The first break-off of the filament occurred from the vicinity of the emerging flux. The emerging flux region appears as a dark spot in the EUV image, because it was hot and hence outside of the EUV pass band. This is verified from the Yohkoh/SXT images, which show the same spot as a bright feature. Yohkoh SXT images also show that the overlying field lines are sheared and hence highly non-potential. After the eruption, the post-flare X-ray loops appeared potential, roughly perpendicular to the neutral line. There was also a tiny cusp-shaped feature at the site of flux emergence visible in the Yohkoh/SXT image, suggesting reconnection between the newly emerging and preexisting fields. The cadence of the Hα pictures was not sufficiently high to see the details of the emerging flux manifestation at the chromospheric level, but a clear arch filament system is evident (See Bruzek, 1967 for details on the arch filament system).

The case study presented above is considered to be a case of flux emergence favorable for reconnection. Feynman and Martin (1995a) investigated a large number of filament eruptions and concluded that two-thirds of all the filament eruptions they studied occurred after substantial amounts of flux emerged in the vicinity of the filament. They also found that about 84% of filaments not associated with flux emergence did not erupt. They further note that the filament invariably erupted when the emerging flux had an orientation favorable for reconnection with the large-scale coronal structures overlying the filament. Green *et al*. (2003) considered the CME and flare productivity of 4 young active regions during their disk passage and found that the majority of CMEs occurred during or after the flux emergence. Numerical simulations by Chen and Shibata (2000) support this interpretation (see Figure 11).

There are exceptions to the scenario presented above. Wang and Sheeley (1999) found 3 cases of flux emergence associated with filament eruption; they also found filament eruptions with no evidence for flux emergence. Subramanian and Dere (2001) studied the solar sources of 32 CMEs observed by SOHO; 41% of the CMEs originated from active regions with no obvious signs of filament eruption. Of the remaining CMEs, 45% from active regions and 15% from quiet regions were associated with filament eruptions. CMEs without filament eruptions originated from young active regions (lifetime $<$3 months), while ARs with filament eruptions

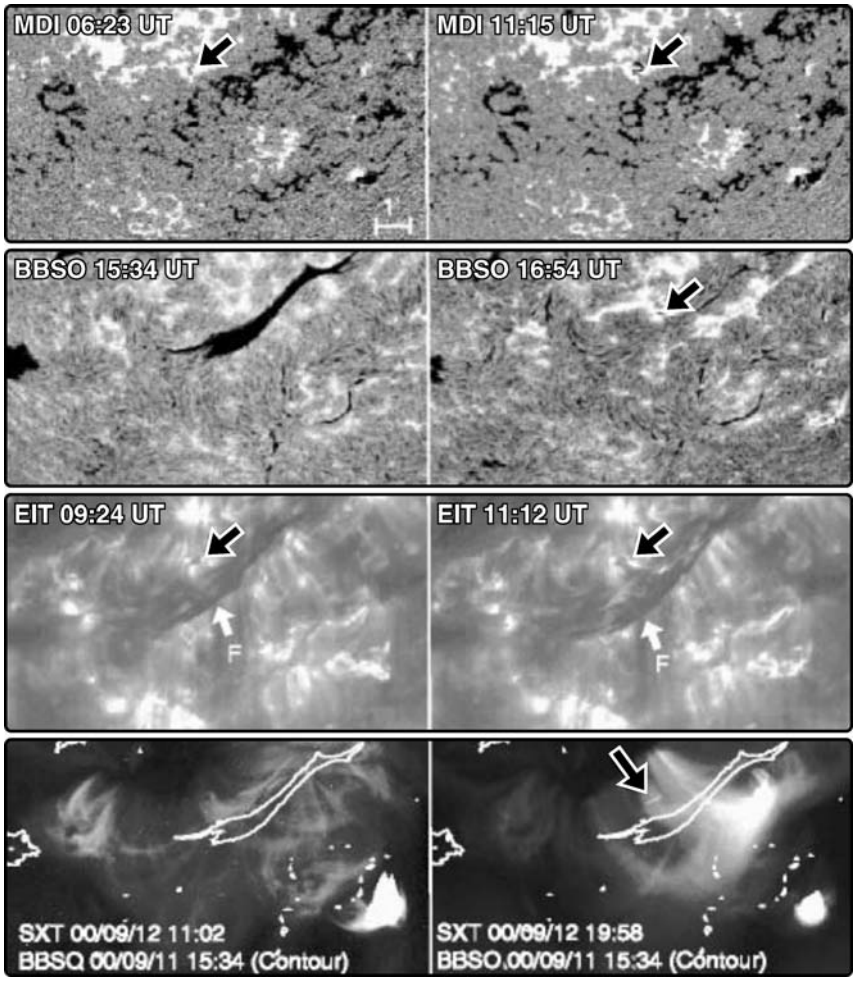

Figure 10. Flux emergence and the associated filament eruption on 2000 September 12. The four rows from top to bottom show pre- and post-eruption pictures at various wavelengths corresponding to various layers from the photosphere to the corona. (top) MDI magnetograms showing the flux emergence to the north of the polarity inversion line as indicated by the arrows. The white and black colors denote the north and south magnetic polarities, respectively. (middle/top) Hα pictures from BBSO showing the pre-eruption filament (shown on the previous day) and the two-ribbon structure in the post eruption stage. The emerging flux region is also indicated showing the arch filament system. (middle/bottom) SOHO/EIT images showing the pre-eruption and erupting stages of the filament (F). Changes in the emerging flux region are also seen. (bottom) Yohkoh/SXT images with the superposed outline of the filament (white contour). The pre-eruption X-ray loops are sheared parallel to the filament and some overlie the filament. In the post-eruption phase the SXT loops are perpendicular to the pre-eruption filament axis.

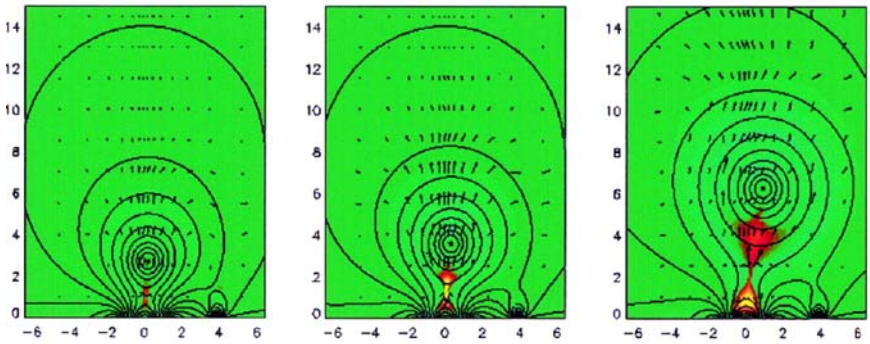

Figure 11. Results of a 2D MHD simulation showing CME eruption following flux emergence at [4,0] to the right of the neutral line (perpendicular to the plane of the paper at the location [0,0]). The solid line represents the magnetic field lines; the arrows indicate the direction and magnitude of flow. The color represents the temperature. (from Chen and Shibata, 2000).

were older (6–7 months). Reconnection-favoring flux emergence seems to be the key aspect in this type of eruption. Lack of flux emergence has to be understood in terms of other types of evolution such as flux cancellation and shearing.

3.4. Helicity Evolution

In recent years the role of helicity injection, or helicity-charging (Rust and Kumar, 1994a,b), has been a focal point in the discussion of eruptive events. In particular, it has been argued that CMEs are the means by which the solar corona expels magnetic helicity accumulated over hours and days by the combination of local shearing motions, differential rotation and the emergence of twisted flux systems (Low, 1996; DeVore, 2000; Démoulin *et al.*, 2002). The attractiveness of magnetic helicity for such studies lies in the fact that it is a globally conserved quantity in ideal MHD and can also be considered to be conserved in resistive MHD on time scales shorter than the global diffusion time scale (Berger, 1984). This property opens up a wide array of possibilities for exploring the CME process both theoretically and observationally (see articles in Brown *et al.*, 1999). An observational manifestation of the connection between helicity and CME production is the soft X-ray sigmoid discussed earlier in this chapter.

Since the solar corona is an open volume with the photosphere as a boundary with normal flux, the magnetic helicity can be transported across the boundary by velocity fields in the photosphere. The Poynting theorem for magnetic helicity, H, in an open volume is given by Berger and Field (1984) as

$$\frac{dH}{dt} = 2\oint (B \cdot A_p) v_z dS - \oint (v \cdot A_p)\, B_z dS$$

where B is the vector magnetic field and v is the velocity vector field (the subscript denoting the vertical component of each of these quantities), A_p is the unique

vector potential of the potential field satisfying the conditions: $\nabla \times A_p \cdot z = B_z$, $\nabla \times A_p = 0$; $A_p \cdot z = 0$. With this definition, H is then the "relative helicity" (Berger and Field, 1984). Thus, the magnetic helicity in an open volume can change either by the passage of field lines through the surface (first term on RHS) or by the horizontal motions of the field lines (second term on RHS).

It is important to consider all potential contributions to the helicity injected into the sigmoid volume. Several studies point to the importance of intrinsic twist in the structures emerging from below the photosphere. Leka *et al.* (1996) showed that most field emerges twisted in a detailed active region study. Moreover, CME studies imply that helicity injection by differential rotation is 2–3 orders of magnitude lower than that required to explain helicity seen in magnetic clouds (Green *et al.*, 2002) and theoretical flux-rope models imply twisting of buoyant flux tubes by convective motions prior to emergence (Fan, 2001). On the other hand, measurement of helicity carried away by CMEs relies on uncertain magnetic cloud measurements and conclusions differ (DeVore, 2000). Strong localized photospheric motions can inject sufficient helicity to drive large flares (Moon *et al.*, 2002).

The emerging flux tube simulations of Magara and Longcope (2001), for example, suggest that neutral-line shear and sigmoidal field arise as a natural by-product of flux emergence with the observed sigmoidal field being the consequence of the emerging inner toroidal field lines of the flux tube. One would also expect a separation and rotation of the opposing polarity regions toward a more axial field orientation. In those cases where flux emergence is found to be important we would need to derive, or estimate, the vertical component of the photospheric flows. This cannot be done directly from observations. However, Kusano *et al.* (2002) have developed an approach which extracts an estimate of the vertical velocity from an inversion of the induction equation, utilizing the observed vector field components and transverse velocity field. Future helicity studies will require detailed measurements of the vector magnetic field and photospheric flow patterns before, during and after significant eruptions. Various approaches to this problem are currently underway at a number of institutions.

3.5. Flux Cancellation

As described previously, the emergence of new magnetic flux, especially in the vicinity of pre-existing magnetic fields, is connected with solar eruptions (e.g., Gaizauskas *et al.*, Zwaan, Feynman and Martin, 1983, 1985, 1995b). Flux cancellation is another mechanism that can trigger CMEs, as discussed by Mikić and Lee (2006, this volume) and by Forbes *et al.* (2006, this volume). The process of flux cancellation has been defined observationally as the mutual disappearance of magnetic fields of opposite polarity at the neutral line separating them (Martin *et al.*, 1985). Flux cancellation has also been identified as a key element in the formation of prominences and filaments (Gaizauskas *et al.*, 1997; Martin, 1998b; Litvinenko and Martin, 1999; van Ballegooijen *et al.*, 2000; Martens and Zwaan, 2001).

Because of the close relationship between flux cancellation and solar eruptions, the role of flux cancellation in prominence formation, eruption, and CME initiation has been studied extensively using numerical models (Linker *et al*., 2001, 2003a,b; Roussev *et al*., 2004b; Amari *et al*., 1999, 2000, 2003b,c; Lionello *et al*., 2002; Welsch *et al*., 2005). These models show that a magnetic configuration subject to flux cancellation can initially exhibit stable behavior with a magnetic field topology that can support prominence material. If flux cancellation is continued beyond a critical value, the configuration erupts. When the configuration is close to the critical state, even a small amount of flux cancellation can trigger a violent eruption. Hence, the triggering event may appear to be unremarkable in photospheric magnetograms.

The halo CME observed on May 12, 1997 illustrates the role of flux cancellation in triggering CMEs. This event occurred during solar minimum when the Sun had a very simple structure. The CME originated from an isolated active region near disk center (AR 8038 at N21W08). The CME was accompanied by a C1.3 flare at 04:42UT. Observations of this event have been analyzed in detail (Plunkett *et al*., 1998; Thompson *et al*., 1998; Webb *et al*., 2000; Gopalswamy and Kaiser, 2002). It has been selected as a SHINE Campaign Event for detailed theoretical study (Gopalswamy, 2005). MDI magnetograms preceding the CME indicate that there is a substantial amount of flux cancellation near the main neutral line in the active region, as shown in Figure 12. Whether this triggered the eruption is a question that is presently being investigated.

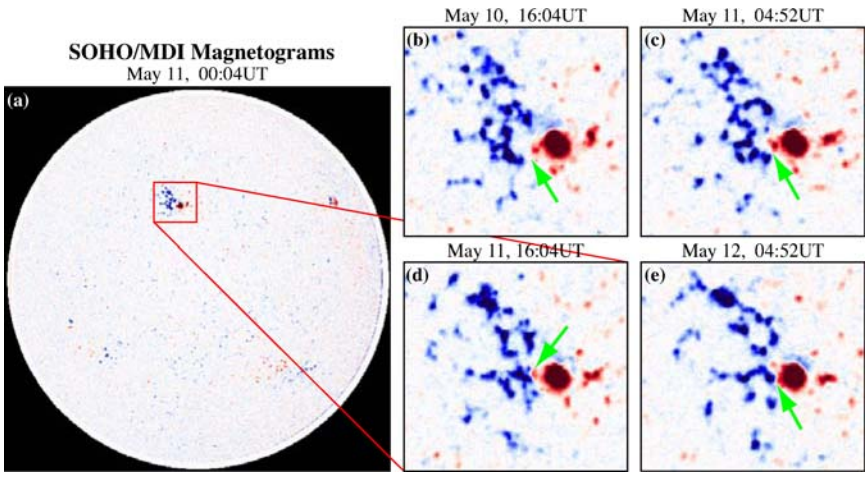

Figure 12. A sequence of MDI magnetograms preceding the halo CME on May 12, 1997. A C1.3 flare occurred at 04:42UT. (a) A full-disk MDI magnetogram showing AR 8038; (b)–(e) detailed magnetograms of the active region approximately 36 hours, 24 hours, and 12 hours prior to eruption, and at the time of eruption. The green arrow indicates an area with substantial convergence of opposite polarity flux at the neutral line, which may have triggered the eruption.

3.6. Successive Eruptions

Some active regions show rapid succession of flares and CMEs over a time scale of minutes to hours. This time scale is too small compared to the typical time scale for energy build-up in active regions. The rapid succession of flares and CMEs therefore represents a fragmented energy release. i.e., all the free energy available in an active region is not released in a single eruption. Many of the SEP-producing active regions are CME-prolific (Gopalswamy *et al*., 2004b). It becomes difficult to distinguish between successive eruptions and a precursor-CME combination. This raises the question whether a preceding eruption makes it easier for the next eruption.

Examination of the angular difference distribution of successive CME pairs indicates an overabundance of these pairs (relative to background levels) when the position angle difference is within 10°; such position-angle coincidence is indicative of successive CMEs from the same source region (Moon *et al*., 2003). Figure 13 shows the heliographic locations of eruptions from AR 9236 and the distribution of flare and CME recurrence times (Gopalswamy *et al*., 2005). Only flares of C-class and above were considered. The average CME recurrence time was 4.6 h with 17 CMEs occurring over a five-day period. Over the same period, there were 33 C, M, and X-class flares with an average recurrence time of 3.6 h. Note that the smallest bins in the CME and flare recurrence distributions contain most of the events. For the CMEs in this bin, it is difficult to identify precursors. The time separation between the two big CMEs was about 10 h. But whether the preceding CMEs have any role in creating the conditions for a subsequent eruption is an open question. For instance, the occurrence of a preceding event might contribute to further destabilization of the source region leading to further eruptions. The active region in Figure 13 was also undergoing dynamic restructuring due to flux emergence in the core of the active region (Nitta and Hudson, 2001), so this region presents one of the best examples to study CME-rich active regions. On the other hand occurrence of a preceding event might contribute to further destabilization of the whole region.

3.7. Streamer Distension

Evolution of coronal streamers as a precursor to CMEs has been considered in the past. Slow addition of mass to the closed field regions of the streamer may result in its subsequent eruption (Wolfson *et al*., 1987) seen as "bugles" (Howard *et al*., 1985; Hundhausen, 1993). Another aspect of this configuration is that the mass in the streamer restrains the cavity, and hence allows for the build-up of sufficient energy to produce eruptions (Wolfson and Saran, 1998). There is also a strong correlation between the direction of propagation of CMEs and the location of streamers, often regardless of the location of the associated eruptive activity at the Sun. As such, streamers may hold clues to understanding the initiation and progression of

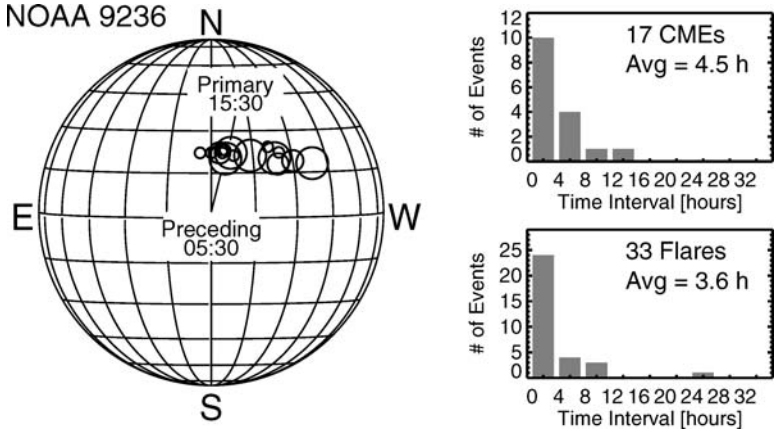

Figure 13. (left) Heliographic coordinates of flares from AR 9236 (November 22–27 2000). The locations and onset times of two halo CMEs on November 24 are also indicated. The size of the circles indicate the flare size (small: C-class, medium: M-class and large: X-class flares). (right) Distributions of time intervals between successive CME (upper) and flares (lower). The average recurrence times are 4.5 h (CMEs) and 3.6 h (flares). A SEP associated halo CME (Primary) at 15:30 UT, was preceded within 10 h by another halo at 05:30 UT on November 25.

CMEs low in the corona. In another kind of streamer evolution, the eruption of the associated prominence is partial and results in some noticeable streamer changes. Gopalswamy *et al.* (2003b) found that about 21% of the slow prominence eruptions were associated with changes in the overlying white-light streamers, instead of CMEs. In these "transverse" prominence eruptions, the prominence material did not reach heights beyond about $0.16R_{\odot}$ above the surface. An interesting result was that the majority of these streamers erupted in the next 4 to 42 hours as CMEs (Gopalswamy *et al.*, 2004a).

Very slow evolution of streamers in brightness and size has been linked to changes in photospheric magnetic flux. In particular, increase in brightness is known to be correlated with decrease in photospheric flux, which was interpreted as opening of flux tubes under the streamer (Poland and MacQueen, 1981). In this sense, we think that the small-scale prominence eruptions produce a similar effect of opening some field lines. Unfortunately, we cannot verify this because it is difficult to observe the photospheric magnetic field changes for limb events. Prolonged coronal dimming associated with some eruptions may also correspond to these field openings (Gopalswamy, 1999). We need a reverse study to look at a large number of streamers as they evolve to arrive at a firm conclusion regarding the connection between the small-scale prominence eruptions and activations on the one hand and the stability of the streamers on the other.

4. Pre-Eruption Energetic Signatures

The energetic signatures preceding the launch of CMEs are transient in nature, unlike the evolutionary signatures discussed in the previous section. The pre-eruption signatures can be thermal or non-thermal. Thermal signatures typically appear as a weak enhancement in the soft X-ray light curve. Imaging observations are essential for checking if these weak enhancements originate from the same source region as the main CME and its associated flare. Non-thermal signatures are primarily observed at radio wavelengths. The radio emission is produced by non-thermal electrons accelerated in the eruption region. The thermal and non-thermal signatures may not be independent because both heating and particle acceleration can occur in the same process such as reconnection. Hard X-ray emission may also result from the non-thermal electrons if they are stopped by dense plasma in the vicinity of the acceleration region. As we noted before, it is sometimes difficult to determine whether the precursor is a separate event or a true precursor, especially when non-thermal emission is involved.

4.1. Thermal Signatures

In addition to the soft X-ray sigmoid signatures discussed above, the pre-eruptive atmosphere shows signatures of an impending eruption in a number of different wavelengths. We have already discussed one example in Section 3.3. Gopalswamy (1999) discussed another filament eruption event associated with a weak halo CME on 1998 January 21. The magnetic field underlying the quiescent filament was very weak. The CME first appeared in the LASCO/C2 field of view at 06:57 UT. Figure 14 shows a set of X-ray structures (marked X) that brightened near the initial location of the filament that subsequently erupted (marked F). There was also a compact brightening in X-rays (not shown) located at the apex of a triangular X-ray structure, which was not observed in EUV images, suggesting that it was indeed a hot structure (Gopalswamy, 2003). The filament completely disappeared about 3 hours after the X-ray brightening. The CME appeared above the southern limb after the filament disappearance.

Recently, Sterling and Moore (2001a) identified EUV structures in the SOHO/EIT data, dubbed EIT crinkles. These structures take the form of small-scale transient sources of emission at a significant distance from the main flaring core. These structures first propagated away from and then faded in towards the central core region. Concurrent with this EUV signature, the soft X-ray emission exhibited faint transient brightening features connecting the main flare core with the location of the EIT crinkles. This indicated that the EUV emission delineates the low temperature foot points of newly heated coronal loops. Based on this evidence Sterling and Moore (2001b) argued that a model akin to the breakout model of Antiochos (1998) and Antiochos *et al*. (1999) best describes the eruptive process in these events.

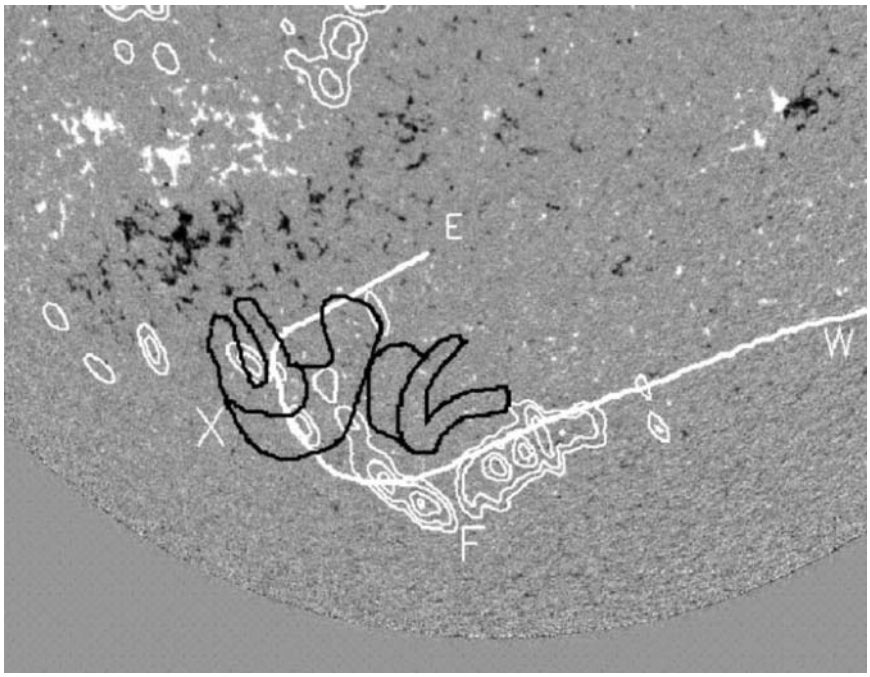

Figure 14. Composite picture of the filament eruption associated with a halo CME on 1998 January 21. The erupting filament (F), observed by the Nobeyama Radioheliograph is shown in white contours. The dark contours (X) define the outline of the initial soft X-ray brightening as observed by Yohkoh/SXT. The elongated neutral line (E) inferred from the MDI magnetogram is also shown. (Adapted from Gopalswamy, 1999).

4.2. NON-THERMAL SIGNATURES

Jackson and Sheridan (1979) found a broad maximum in the number of isolated metric-wave Type III bursts about 5 h prior to large H_α solar flares. The maximum was more pronounced if only the type III bursts co-located with the flare are considered. A similar result was obtained when they considered type III bursts prior to CME onsets (Jackson *et al*., 1978). From these works, they concluded that the Type III burst activity was a good indicator of coronal energy input and storage near the time of a major eruption. Type III bursts are caused by mildly relativistic electrons, so they are non-thermal in nature and might represent small-scale energy releases. Kundu *et al*. (1987) used a single event with radio imaging to show that precursor type III bursts occur at the same location as the main flare and suggest that small-scale reconnection occurred continuously starting about 1 h before the flare.

It is possible to investigate the behavior of filaments and their cavities using weak non-thermal radio bursts which precede filament eruptions. Figure 15 presents an event observed on 1999 September 2 where a small filament in the vicinity of an

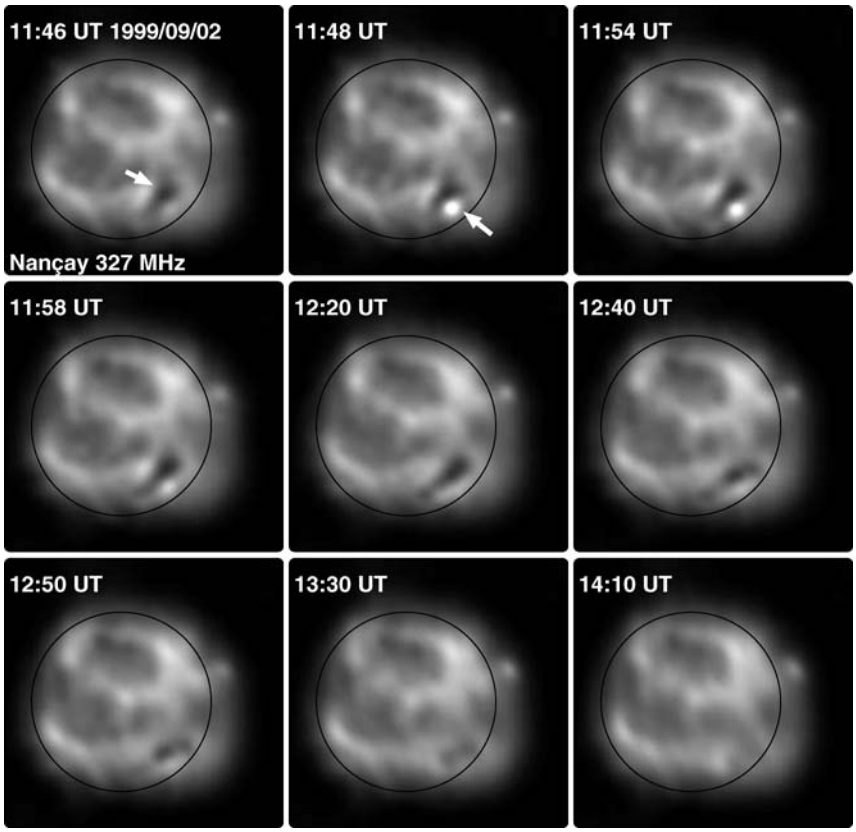

Figure 15. Nançay Radioheliograph observations at 327 MHz showing the slow evolution of a filament cavity, indicated by an arrow on the 11:46 UT image, linked with changes seen in white light streamers. The onset of the changes seen in the radio cavity (slow distension and fading) coincide with bright non-thermal bursts, indicated by an arrow on the 11:48 UT image, seen in the vicinity of the filament cavity, starting at about 11:48 UT and lasting roughly 10 min at 327 MHz. (Adapted fom Marqué, 2004.)

active region erupted (Marqué, 2004). The earliest signatures of the event were faint non-thermal bursts occurring on the side of the cavity and lasting for about 10 min. Following the radio bursts the cavity distended and slowly faded away, implying a slow eruption.

Repeated acceleration of electrons at multiple locations underlying a coronal streamer was reported by Klein *et al*. (1997), as inferred from type III bursts. A few hours after the start of these type III bursts, the streamer erupted. The type III bursts (reverse and normal drift) were also coincident with soft X-ray brightenings. These authors suggest that the type III bursts are indicative of pre-eruption instabilities in the large-scale structure that eventually erupts. See Pick *et al*. (2006, this volume) for a discussion of radio signatures occurring in the eruptive phase of CMEs.

Non-thermal signatures in hard X-rays and decimetric spikes preceding the main eruption by about 2 h was reported during the September 24, 2001 CME (Fárník *et al*., 2003). There were also accompanying thermal signatures in the form of GOES soft X-ray enhancements. About 1 h before the main eruption, an unusual drifting radio continuum was observed together with two radio sources (at 327 and 164 MHz) in positions corresponding to expanding loops seen in Yohkoh/SXT and SOHO/EIT images, accompanied by a filament disappearance during the same period. Expanding loops and filament disappearance are characteristics of a preceding CME, but it is unlikely that such a preceding CME would be observed in white light because of the disk center location of the eruption and a major CME from the same region within an hour. Events like this demonstrate the complexity in understanding the precursors, because one might have to consider smaller preceding CMEs as part of the pre-event evolution.

4.3. Submillimeter Pulsations

Rapid (subsecond) pulsating bursts at submillimeter wavelengths have been found to be closely associated with CME launch times (Kaufmann *et al*., 2003). Figure 16 shows an example of a submillimeter pulsating burst on 2001 December 13. The wavelet decomposition scalogram at 212 GHz shows the submillimeter activity preceding the CME launch by several minutes.

The submillimeter pulsating bursts may or may not have an associated impulsive bulk emission. A sample of 20 such pulsating events were analyzed in more detail, and all of them exhibited similar onset of the pulsating bursts before CME launch times. It is not possible to establish accurate statistics because the definition of the pulse onset times depends on the telescope sensitivity, which is highly variable due to atmospheric transmission conditions for different observations. However, there is no doubt that the onset times of the submillimeter pulsating bursts precede the CME launch times by a few to tens of minutes. The origin of these rapid pulses is unknown. Their association with the pre-CME conditions is significant, which needs to be further investigated by more observations covering a wider range of frequencies, and by theoretical interpretation on the possible physical mechanisms involved.

4.4. Prolonged Transequatorial Dimming

During 1998 April 27–May 9, a series of transequatorial eruptions occurred involving a major active region in the southern hemisphere (AR 8210) and a smaller region in the northern hemisphere. The first major eruption was a fast (1385 km/s) CME on 1998 April 27 appearing at 08:56 UT in the SOHO/LASCO FOV (Gopalswamy *et al*., 1999). From the height-time plot, the CME onset was estimated to occur within 08:45–08:55 UT. About 2 h before the CME onset, the

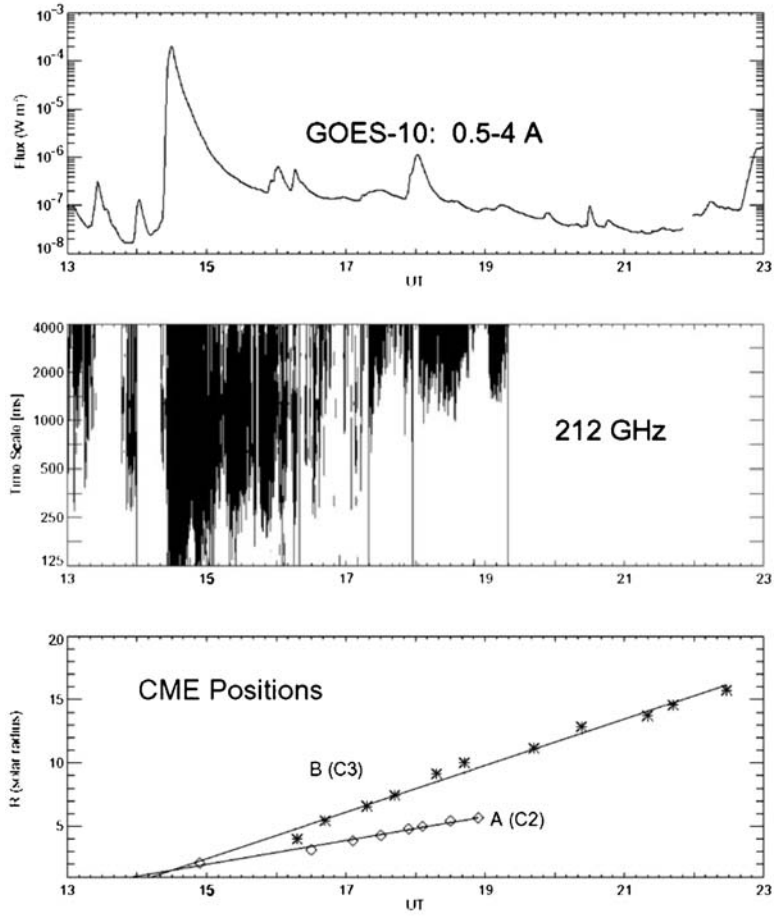

Figure 16. GOES soft ray light curve (top), millisecond pulsations observed at 212 GHz (middle) and the height-time plots of two associated CMEs labeled A (observed by LASCO C2) and B (observed by LASCO C3). The CME onsets coincided with small GOES soft X-ray spike and associated millisecond pulsations.

transequatorial region started showing weak dimming for about an hour (06:42 to 08:06 UT) followed by a deeper dimming (see Figure 17) that reached a maximum at about 08:45 UT, coinciding with the projected onset of the CME.

Figure 18 shows the EUV intensity in the active region (AR) and the transequatorial region (D), compared with the GOES soft X-ray light curve (G). The flare itself started only at 08:55 UT (see the curves AR and G). The CME was already at a height of $2.6 R_{\odot}$ at 08:56 UT, just one minute after the flare onset. The CME must have traveled a distance of 1.6 Ro in 15 min before the start of the flare, which gives an average speed of 1237 km/s, consistent with that obtained from the height-time plot. Another interesting aspect of this event is that there was a long wavelength

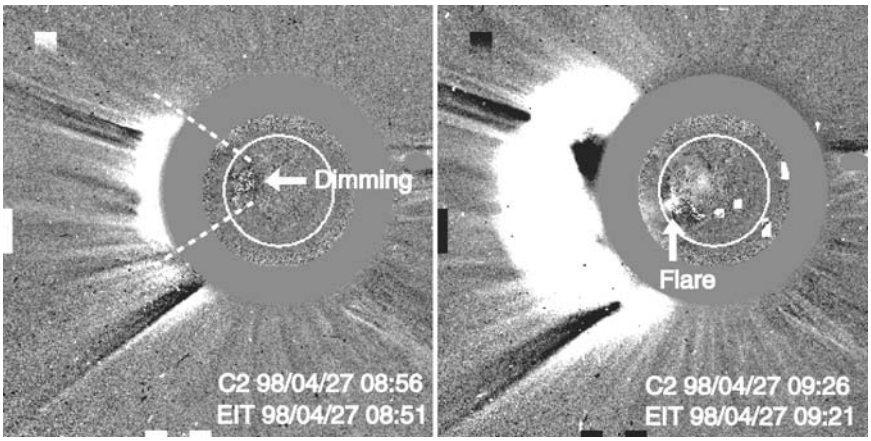

Figure 17. (left) SOHO/LASCO CME on 1998 April 27, which appeared first above the occulting disk at 08:56 UT. The angular extent of the CME can be seen to be consistent with the extent of the transequatorial dimming observed by SOHO/EIT. (right) The CME in the next frame with the associated flare in AR 8210. The projected onset of the CME is estimated to occur within 08:45–08:51 UT from the height-time plots. Note the widespread disturbance in the transequatorial region in the EIT difference image at 09:21 UT.

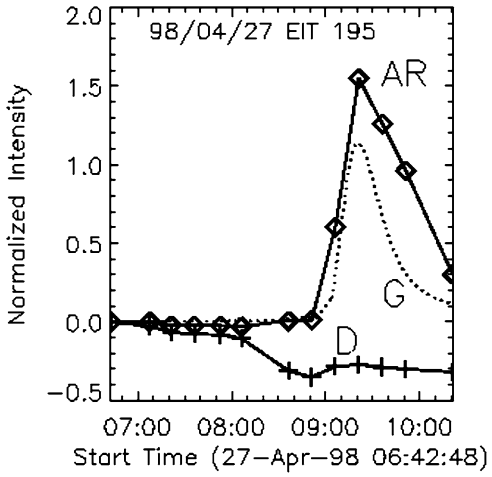

Figure 18. SOHO/EIT 195 Å light curve showing the EUV intensity in the active region (AR) and the transequatorial dimming region (D) compared with the GOES soft X-ray light curve (G) on 1998 April 27. The flare emission starts only at 08:45 UT in AR 8210, whereas the dimming had started two hours earlier. The CME onset was about 40 min before the flare onset.

(<14 MHz) type III burst when the weak dimming started, and a series of type III bursts at the start of the deep dimming, leading up to the intense complex type III bursts at the time of the flare. The dimming and the weak type III bursts may be indicative of the subsequent eruption. However, Khan and Hudson (2000) came to

the opposite conclusion for three eruptions that occurred when AR 8210 was on the western hemisphere. They suggested that flares from AR 8210 produced blast waves whose impact caused the eruption of the transequatorial structure.

5. Global Issues

In this section, we discuss two related issues regarding the nature of the pre-eruption configurations of the source regions: (i) the prominence configuration (normal and inverse polarity) that might lead to possible two types of CMEs, and (ii) the high-latitude CMEs associated with polar crown prominences. The high-latitude CMEs are clearly prominence related, while the low-latitude ones can be either flare related or prominence related. While the distinction between the two types may not be significant as far as the initiation mechanism is concerned, it may be important in the context of the solar polarity reversal. The high-latitude CMEs are purely prominence related, whereas the low-latitude CMEs are mostly active-region (and hence flare) related. The high-latitude CMEs are related to solar polarity reversal.

5.1. Normal and Inverse Polarity CMEs

MacQueen and Fisher (1983) had suggested that different acceleration mechanisms may be operating in CMEs associated with prominence eruptions and flares. The flare-related CMEs are characterized by higher constant speed, while the prominence-related CMEs are slower and accelerating (see also St. Cyr *et al*., 1999). (Tappin and Simnett, 1997) used 149 LASCO CMEs and found that the constant speed CMEs were generally faster. Examples of height-time profiles showing constant speed and accelerating CMEs were also reported by others (Sheeley *et al*., 1999; Andrews and Howard, 2001; Gopalswamy *et al*., 2001). Moon *et al*. (2002) also found a clear difference in speeds of flare-related (759 km/s) and prominence-related (513 km/s) CMEs. The flare-related CMEs also showed a tendency for deceleration, but this probably reflects the fact that they are faster (Gopalswamy *et al*., 2001). The question is whether the speed difference represents a qualitative distinction between the two types of CMEs. Studying the acceleration of CMEs, Chen and Krall (2003) concluded that one mechanism is sufficient to explain flare- and prominence-related CMEs. Furthermore, the distinction between the two is somewhat ambiguous because flares often involve prominence eruptions and quiescent prominence eruptions result in two-ribbon flares. The primary distinction may be the strength of the magnetic fields and the inverse and normal polarity configurations in the pre-eruption stage. In fact, two different pre-eruption prominence configurations have been suggested as the basic reason for the two types of CMEs, accelerating and constant-speed (Low and Zhang, 2002). These authors assume that the flux rope is a basic ingredient in both configurations. They propose that

loss of equilibrium of the flux ropes is the mechanism that initiates CMEs (Low, 1996). In the pre-eruptive state, the flux rope is held down by the prominence mass and the magnetic tension of the overlying fields. A CME is produced when the confinement of the flux rope breaks down for a variety of reasons, such as loss of prominence mass (Low and Zhang, 2002). The interaction between the current in the flux rope and the current sheets in the overall configuration determines the nature of the eruption and the dynamics of the flux rope. (Low and Zhang, 2002) claim that the differences in this interaction can account for the predominance of accelerating CMEs from inverse polarity configurations and constant speed CMEs from normal polarity configurations.

5.2. High-Latitude CMEs and Polarity Reversal

As we discussed before, the presence of a closed field structure on the Sun is a basic requirement for CMEs. The number of closed field regions on the Sun depends on the phase of the solar cycle. During solar minimum, most of the closed field regions are confined to the equatorial streamer belt. As the solar cycle progresses, closed field regions spread to all latitudes. This is often reflected in the tilt angle of the heliospheric current sheet. The sunspot number is often used as a measure of solar activity, but it is not a good indicator of CMEs especially during solar maximum. This is reflected in the less-than-perfect correlation between the CME rate and sunspot number. The main reason is that solar activity defined by sunspots is confined to lower latitudes ($< 45^\circ$). There is another source of CMEs, especially during the rising and maximum phases of the solar cycle: the polar crown filaments (PCFs). It is well known that the PCFs begin appearing at the poles in the rising phase and disappear somewhere during the maximum of activity (see Cliver *et al.*, 1994). No sunspots are associated with the PCFs, so the PCF-related CMEs (or high-latitude CMEs) are not expected to be correlated with sunspot activity. The rate of high-latitude CMEs is clearly related to the migration of closed field structures to the poles. A close temporal relationship between the cessation of high-latitude CMEs and the polarity reversal at the solar poles has been demonstrated for solar cycles 21 and 23 (Gopalswamy *et al.*, 2003a). Typically, the high-latitude CME rate falls to the background value just before the reversal in each pole. High-latitude CMEs provide a natural explanation for the disappearance of PCFs, which need to be removed before the poles can develop an open field structure of the opposite polarity.

6. Discussion, Summary and Future Perspectives

So far we have discussed observations and interpretations of the three basic aspects of the pre-CME Sun: pre-eruption structure, evolution, and energetic

signatures. In this section, we briefly discuss how these observations are being used in numerical modeling of CME initiation. Then we shall present a summary and future perspectives.

6.1. Observational Input to CME Initiation Models

The main observational inputs for modeling CME initiation have been photospheric magnetic field measurements, especially from vector magnetograms. Particularly useful are sequences of magnetic measurements that can be used to model the storage of energy, the build-up of twist, and possibly the crossing of a stability threshold.

The development of CME initiation models hinges principally on our understanding of the detailed structure and evolution of the coronal magnetic field in the pre-eruptive state (e.g., Mikić and Lee, 2006, this volume; Forbes *et al.*, 2006, this volume). Unfortunately, it is difficult to measure coronal magnetic fields in detail, so we have to rely on photospheric measurements, extrapolated into the corona using model fields. Moreover, at present we routinely only measure these magnetic fields using (longitudinal) magnetographs, which only supply one component of the magnetic field (the normal component at disk center). The energization of coronal fields can only be determined from vector magnetic field measurements, and this information has been scant.

We have had to rely on inferences of magnetic structure, principally from X-ray and EUV emission. The high-resolution EUV images from the TRACE mission have been especially useful in this regard, since they tend to emphasize what appear to be traces of individual magnetic field lines. At times, white-light coronagraph images, and especially movies, can help us infer the pre- and post-eruptive structure of CMEs. The twist of embedded filaments is sometimes clearly visible in coronagraph movies of streamer eruptions. Radio emission measurements may be used to infer the strength, and to a more limited extent the direction, of the coronal magnetic field. Of course, these qualitative morphological indications of the magnetic field geometry are not suitable for detailed modeling purposes. Our poor knowledge of CME initiation is largely a consequence of our limited ability to measure the coronal magnetic field.

Fortunately, two upcoming missions will greatly help in this regard. STEREO will image the corona in EUV and white light from two different vantage points, which, in combination with observations from SOHO, TRACE, and the ground, will help to deconvolve projection effects and help us to understand the three-dimensional nature of coronal features. Solar B will for the first time measure vector magnetic fields at high resolution from space, as well as X-ray emission at high resolution. These observations are expected to greatly advance our understanding of CME initiation.

6.2. Summary and Future Perspectives

Appearance of a large-scale closed magnetic field structure on the Sun can be considered as the lowest form of pre-CME evolution necessary for a CME. Thus, the ability of the Sun to emerge closed field structure from below the photosphere into the atmosphere is a basic requirement for a CME. Active regions and filament channels are the basic units of closed field structures, which often occur together and in clusters. During solar maximum, a large number of these structures are present on the Sun with a correspondingly higher CME rate. Also the latitudinal distribution of the magnetic regions, governing the locations of eruptions on the Sun, are different between solar maximum and minimum. For example, polar crown eruptions occur starting a couple of years before the solar polarity reversal and then practically disappear after that. Next, the magnetic source region has to build-up free energy. Identification of the signatures of this energy build-up is a crucial step in deciding whether and when a CME will occur. Flux emergence and cancellation, shear and converging flows are some of the photospheric signatures that indicate energy build-up. During the build-up phase, minor energetic events occur, which are denoted as precursors or pre-eruption energy release. Both thermal (soft X-rays, EUV, Hα) and non-thermal (radio, hard X-rays) precursors have been observed. Sometimes it is difficult to decide whether a pre-eruption energy release is a true precursor or a separate eruption. Even a prior smaller eruption may lead to a bigger subsequent eruption by destabilizing the larger structures in the eruption region. While this simplified picture provides insight, the reality is more complex and we are far from predicting whether an active region is likely to erupt by looking at its evolution prior to eruption. Progress needs to be made in answering a number of open questions regarding the role of flux ropes in CMEs: When are they formed, before or during eruption? If flux ropes form before eruption, do they formed in the atmosphere or do they form in the subsurface layers and then subsequently emerge? Do all CMEs involve flux ropes? An answer in the affirmative would simplify the modeling of CMEs. Unfortunately, there is an observational difficulty. While the filament or coronal cavity overlying quiescent prominences is often thought to be a flux rope, it is hard to observe cavities overlying active region filaments. It is important to know whether active-region filaments have cavities or not. Cavities are well observed only in CMEs associated with filament eruptions. In disk CMEs, however, we often observe only two parts: the frontal structure and the bright core. Is this difficulty in observing cavities a projection effects or because they do not exist? For example, radio observations often show the eruption of cavities from the solar disk, suggesting that they are coherent structures. Is the filament a flux rope as some modelers assume? Why are some CMEs not associated with filaments/filament eruptions? Other questions pertaining to the evolution of the pre-eruptive structures towards eruption also required detailed study: What is the role of flux emergence/cancellation/shear in flux-rope formation and CME initiation? What are the observed characteristics of the source of fast CMEs and how do they

differ from those of slow CMEs? What is the location of reconnection with respect to the filament?

We have made enormous progress in understanding the gross properties of CMEs, thanks to the continuous and uniform observations of high quality from the SOHO mission. Yet, the observational coverage of the early life of CMEs is limited, mainly due to the poor cadence of observations. For example, the CME watch in EUV (195 Å) has a cadence of 12 min over a very limited field of view, preventing us from having a close look at CME initiation and early evolution. High cadence images are needed to systematically identify pre-eruption signatures, which is crucial in developing tools to predict the impending onset of CMEs. We still lack quantitative understanding in connecting magnetic complexity in a source region to CME productivity. Since vector magnetograms provide most of the information on the free energy available in active regions, they should be integrated with MHD models. Finally, a better understanding of the helioseismic subsurface imaging of active regions might provide important clues to the build-up of energy in active regions.

Acknowledgements

The open data policy of the SOHO project has contributed enormously in the CME-related studies. We thank S. Yashiro for helping with some of the figures.

References

Abbett, W. P., and Fisher, G. H.: 2003, *Astrophys. J.* **582**, 475–485.
Adams, W. M.: 1976, *Sol. Phys.* **47**, 601–605.
Amari, T., Luciani, J. F., Aly, J. J., Mikić, Z., and Linker, J.: 2003a, *Astrophys. J.* **585**, 1073–1086.
Amari, T., Luciani, J. F., Aly, J. J., Mikić, Z., and Linker, J.: 2003b, *Astrophys. J.* **585**, 1073–1086.
Amari, T., Luciani, J. F., Aly, J. J., Mikić, Z., and Linker, J.: 2003c, *Astrophys. J.* **595**, 1231–1250.
Amari, T., Luciani, J. F., Mikić, Z., and Linker, J.: 1999, *Astrophys. J.* **518**, L57–L60.
Amari, T., Luciani, J. F., Mikić, Z., and Linker, J.: 2000, *Astrophys. J.* **529**, L49–L52.
Ambastha, A.: 1998, *ASP Conf. Ser. 140: Synoptic Solar Physics*. pp. 113–119.
Andrews, M. D., and Howard, R. A.: 2001, *Space Science Reviews* **95**, 147–163.
Antiochos, S. K.: 1998, *Astrophys. J.* **502**, L181.
Antiochos, S. K., DeVore, C. R., and Klimchuk, J. A.: 1999, *Astrophys. J.* **510**, 485–493.
Babcock, H. W., and Babcock, H. D.: 1955, *Astrophys. J.* **121**, 349–366.
Berger, M. A.: 1984, *Geophys. Astrophys. Fluid Dynam.* **30**, 79–104.
Berger, M. A., and Field, G. B.: 1984, *J. Fluid Mechan.* **147**, 133–148.
Berger, T. E., Loefdahl, M. G., Shine, R. S., and Title, A. M.: 1998, *Astrophys. J.* **495**, 973–983.
Bhatnagar, A.: 1996, *Ap&SS* **243**, 105–112.
Bravo, S.: 1996, *Advances in Space Research* **17**, 285–288.
Brown, D. S., Nightingale, R. W., Alexander, D., Schrijver, C. J., Metcalf, T. R., Shine, R. A., *et al.*: 2003, *Sol. Phys.* **216**, 79–108.
Brown, M. R., Canfield, R. C., and Pevtsov, A. A. (eds.): 1999, Magnetic Helicity in Space and Laboratory Plasmas.
Bruzek, A.: 1967, *Sol. Phys.* **2**, 451–461.
Burlaga, L., Fitzenreiter, R., Lepping, R., Ogilvie, K., Szabo, A., Lazarus, A., *et al.*: 1998, *J. Geophys. Res.* **103**, 277–286.

Canfield, R. C., Hudson, H. S., and McKenzie, D. E.: 1999, *Geophys. Res. Lett.* **26**, 627–630.
Canfield, R. C., Hudson, H. S., and Pevtsov, A. A.: 2000, *IEEE Transactions on Plasma Science*, December 2000 **28**, 1786–1794.
Canfield, R. C., and Pevtsov, A. A.: 1998, *ASP Conf. Ser. 140: Synoptic Solar Physics* pp. 131–143.
Canfield, R. C., Priest, E. R., and Rust, D. M.: 1974, *High Altitude Observatory, CO: Flare Related Magnetic Field Dynamics*, pp. 361–371.
Chen, J., Howard, R. A., Brueckner, G. E., Santoro, R., Krall, J., Paswaters, S. E., *et al.*: 1997, *Astrophys. J.* **490**, L191.
Chen, J., and Krall, J.: 2003, *J. Geophys. Res. (Space Phys.)* 2–1.
Chen, P. F., and Shibata, K.: 2000, *Astrophys. J.* **545**, 524–531.
Cliver, E. W., St. Cyr, O. C., Howard, R. A., and McIntosh, P. S.: 1994, *IAU Colloq. 144: Solar Coronal Struct.* pp. 83–89.
Cremades, H., and Bothmer, V.: 2004, *A&A* **422**, 307–322.
Démoulin, P., Mandrini, C. H., van Driel-Gesztelyi, L., Thompson, B. J., Plunkett, S., Kovári, Z., *et al.*: 2002, *A&A* **382**, 650–665.
Delannée, C., and Aulanier, G.: 1999, *Sol. Phys.* **190**, 107–129.
Démoulin, P., Henoux, J. C., Mandrini, C. H., and Priest, E. R.: 1997, *Sol. Phys.* **174**, 73–89.
Dere, K. P., Brueckner, G. E., Howard, R. A., Michels, D. J., and Delaboudiniere, J. P.: 1999, *Astrophys. J.* **516**, 465–474.
DeVore, C. R.: 2000, *Astrophys. J.* **539**, 944–953.
Dobrzycka, D., Cranmer, S. R., Raymond, J. C., Biesecker, D. A., and Gurman, J. B.: 2002, *Astrophys. J.* **565**, 621–629.
Engvold, O.: 1988, *Solar and Stellar Coronal Structure and Dynamics*, pp. 151–169.
Fárník, F., Hudson, H. S., Karlický, M., and Kosugi, T.: 2003, *A&A* **399**, 1159–1166.
Fan, Y.: 2001, *Astrophys. J.* **554**, L111–L114.
Feynman, J., and Martin, S. F.: 1995a, *J. Geophys. Res.* **100**, 3355–3367.
Feynman, J., and Martin, S. F.: 1995b, *J. Geophys. Res.* **100**, 3355–3367.
Filippov, B. P., Gopalswamy, N., and Lozhechkin, A. V.: 2001, *Sol. Phys.* **203**, 119–130.
Forbes, T. G.: 2000, *J. Geophys. Res.* **105**, 23153–23166.
Forbes, T. G., J. A. Linker, *et al.*: 2006, *Space Sci. Rev.* this volume, doi: 10.1007/s11214-006-9019-8.
Gaizauskas, V., Harvey, K. L., Harvey, J. W., and Zwaan, C.: 1983, *Astrophys. J.* **265**, 1056–1065.
Gaizauskas, V., Zirker, J. B., Sweetland, C., and Kovacs, A.: 1997, *Astrophys. J.* **479**, 448–457.
Gibson, S. E., Fletcher, L., Del Zanna, G., Pike, C. D., Mason, H. E., Mandrini, C. H., *et al.*: 2002, *Astrophys. J.* **574**, 1021–1038.
Gilbert, H. R., Holzer, T. E., Burkepile, J. T., and Hundhausen, A. J.: 2000, *Astrophys. J.* **537**, 503–515.
Glover, A., Harra, L. K., Matthews, S. A., and Foley, C. A.: 2003, *A&A* **400**, 759–767.
Gopalswamy, N.: 1999, in: Bastian, T. S., Gopalswamy, N., and Shibasaki, K. (eds.), *Proceedings of the Nobeyama Symposium, held in Kiyosato, Japan, Oct. 27–30, 1998*, NRO Report No. 479., pp. 141–152.
Gopalswamy, N.: 2003, *Adv. Space Res.* **31**, 869–881.
Gopalswamy, N.: 2005, *EOS Trans. AGU* **86**(50), 525.
Gopalswamy, N., Hanaoka, Y., and Hudson, H. S.: 2000, *Adv. Space Res.* **25**, 1851–1854.
Gopalswamy, N., Hanaoka, Y., Kosugi, T., Lepping, R. P., Steinberg, J. T., Plunkett, S., *et al.*: 1998, *Geophys. Res. Lett.* **25**, 2485–2488.
Gopalswamy, N., and Kaiser, M. L.: 2002, *Adv. Space Res.* **29**, 307–312.
Gopalswamy, N., Lara, A., Yashiro, S., and Howard, R. A.: 2003a, *Astrophys. J.* **598**, L63–L66.
Gopalswamy, N., Shimojo, M., Lu, W., Yashiro, S., Shibasaki, K., and Howard, R. A.: 2003b, *Astrophys. J.* **586**, 562–578.
Gopalswamy, N., Shimojo, M., Lu, W., Yashiro, S., Shibasaki, K., and Howard, R. A.: 2004a, *Adv. Space Res.* **33**, 676–680.

Gopalswamy, N., White, S. M., and Kundu, M. R.: 1991, *Astrophys. J.* **379**, 366–380.
Gopalswamy, N., Yashiro, S., Kaiser, M. L., Howard, R. A., and Bougeret, J.-L.: 2001, *J. Geophys. Res.* **106**(15), 29219–29230.
Gopalswamy, N., Yashiro, S., Kaiser, M. L., Thompson, B. J., and Plunkett, S.: 1999, in: Bastian, T. S., Gopalswamy, N., and Shibasaki, K. (eds) *Proceedings of the Nobeyama Symposium, held in Kiyosato, Japan, Oct. 27-30, 1998, NRO Report No. 479,* pp. 207–210.
Gopalswamy, N., Yashiro, S., Krucker, S., and Howard, R. A.: 2005, Dere, K., Wang, J., and Yan, Y. (eds.), *IAU Symposium*, pp. 367–373.
Gopalswamy, N., Yashiro, S., Krucker, S., Stenborg, G., and Howard, R. A.: 2004b, *Journal of Geophysical Research (Space Physics)* **109**(A18), 12105.
Gosling, J. T., Birn, J., and Hesse, M.: 1995, *Geophys. Res. Lett.* **22**, 869–872.
Green, L. M., Démoulin, P., Mandrini, C. H., and Van Driel-Gesztelyi, L.: 2003, *Sol. Phys.* **215**, 307–325.
Green, L. M., López fuentes, M. C., Mandrini, C. H., Démoulin, P., Van Driel-Gesztelyi, L., and Culhane, J. L.: 2002, *Sol. Phys.* **208**, 43–68.
Hagyard, M. J., Moore, R. L., and Emslie, A. G.: 1984, *Adv. Space Res.* **4**, 71–80.
Hanaoka, Y., Kurokawa, H., Enome, S., Nakajima, H., Shibasaki, K., Nishio, M., *et al.*: 1994, *PASJ* **46**, 205–216.
Harvey, K. L., and Harvey, J. W.: 1976, *Sol. Phys.* **47**, 233–246.
Hori, K., and Culhane, J. L.: 2002, *A&A* **382**, 666–677.
House, L. L., Illing, R. M. E., Sawyer, C., and Wagner, W. J.: 1981, *BASS* **13**, 862.
Howard, R. A., Sheeley, N. R., Michels, D. J., and Koomen, M. J.: 1985, *J. Geophys. Res.* **90**, 8173–8191.
Hudson, H. S., Acton, L. W., Harvey, K. L., and McKenzie, D. E.: 1999, *Astrophys. J.* **513**, L83–L86.
Hundhausen, A. J.: 1993, *J. Geophys. Res.* **98**, 13177–13200.
Illing, R. M. E., and Hundhausen, A. J.: 1985, *J. Geophys. Res.* **90**(9), 275–282.
Jackson, B. V., and Sheridan, K. V.: 1979, *Proc. Astron. Soc. Aust.* **3**, 383–386.
Jackson, B. V., Sheridan, K. V., Dulk, G. A., and McLean, D. J.: 1978, *Proc. Astronom. Soc. Aust.* **3**, 241.
Kaufmann, P., Giménez de Castro, C. G., Makhmutov, V. S., Raulin, J., Schwenn, R., Levato, H., *et al.*: 2003, *J. Geophys. Res. (Space Phys.)* **108**, 5–1.
Khan, J. I., and Hudson, H. S.: 2000, *Geophys. Res. Lett.* **27**, 1083–1086.
Klein, K.-L., Aurass, H., Soru-Escaut, I., and Kalman, B.: 1997, *A&A* **320**, 612–619.
Kopp, R. A., and Pneuman, G. W.: 1976, *Sol. Phys.* **50**, 85–98.
Krall, K. R., Smith, J. B., Hagyard, M. J., West, E. A., and Cummings, N. P.: 1982, *Sol. Phys.* **79**, 59–75.
Kundu, M. R., Gopalswamy, N., Saba, J. L. R., Schmelz, J. T. S., and Strong, K. T.: 1987, *Sol. Phys.* **114**, 273–288.
Kundu, M. R., and McCullough, T. P.: 1972, *Sol. Phys.* **24**, 133–141.
Kuperus, M., and van Tend, W.: 1981, *Sol. Phys.* **71**, 125–139.
Kusano, K., Maeshiro, T., Yokoyama, T., and Sakurai, T.: 2002, *Astrophys. J.* **577**, 501–512.
Lara, A., Gopalswamy, N., and Deforest, C.: 2000, *Geophys. Res. Lett.* **27**, 1435–1438.
Leamon, R. J., Canfield, R. C., Blehm, Z., and Pevtsov, A. A.: 2003, *Astrophys. J.* **596**, L255–L258.
Leamon, R. J., Canfield, R. C., and Pevtsov, A. A.: 2002, *J. Geophys. Res. (Space Phys.)*, pp. 1–1.
Leka, K. D., Canfield, R. C., McClymont, A. N., and van Driel-Gesztelyi, L.: 1996, *Astrophys. J.* **462**, 547.
Liggett, M., and Zirin, H.: 1984, *Sol. Phys.* **91**, 259–267.
Linker, J. A., Lionello, R., Mikić, Z., and Amari, T.: 2001, *J. Geophys. Res.* **106**, 25165–25176.
Linker, J. A., Mikić, Z., Lionello, R., Riley, P., Amari, T., and Odstrcil, D.: 2003a, *Phys. Plasmas* **10**, 1971–1978.

Linker, J. A., Mikić, Z., Riley, P., Lionello, R., and Odstrcil, D.: 2003b, in: Velli, M., Bruno, R., and Malara, F. (eds.), *AIP Conference Proceedings: Solar Wind Ten*, American Institute of Physics, New York, vol. 679, pp. 703–710.
Lionello, R., Mikić, Z., Linker, J. A., and Amari, T.: 2002, *Astrophys. J.* **581**, 718–725.
Litvinenko, Y. E., and Martin, S. F.: 1999, *Sol. Phys.* **190**, 45–58.
Longcope, D. W.: 2004, *Astrophys. J.* **612**, 1181–1192.
Low, B. C.: 1996, *Sol. Phys.* **167**, 217–265.
Low, B. C., and Hundhausen, J. R.: 1995, *Astrophys. J.* **443**, 818–836.
Low, B. C., and Zhang, M.: 2002, *Astrophys. J.* **564**, L53–L56.
Mackay, D. H., Gaizauskas, V., Rickard, G. J., and Priest, E. R.: 1997, *Astrophys. J.* **486**, 534–549.
MacQueen, R. M., and Fisher, R. R.: 1983, *Sol. Phys.* **89**, 89–102.
Magara, T., and Longcope, D. W.: 2001, *Astrophys. J.* **559**, L55–L59.
Marqué, C.: 2004, *Astrophys. J.* **602**, 1037–1050.
Marqué, C., Lantos, P., and Delaboudinière, J. P.: 2002, *A&A* **387**, 317–325.
Martens, P. C., and Zwaan, C.: 2001, *Astrophys. J.* **558**, 872–887.
Martin, S. F.: 1998a, *Sol. Phys.* **182**, 107–137.
Martin, S. F.: 1998b, *Sol. Phys.* **182**, 107–137.
Martin, S. F., Livi, S. H. B., and Wang, J.: 1985, *Aust. J. Phys.* **38**, 929–959.
Marubashi, K.: 1986, *Adv. Space Res.* **6**, 335–338.
Metcalf, T. R., Jiao, L., McClymont, A. N., Canfield, R. C., and Uitenbroek, H.: 1995, *Astrophys. J.* **439**, 474–481.
Metcalf, T. R., Leka, K. D., and Mickey, D. L.: 2004, *Am. Astron. Soc. Meeting Abstracts* **204**.
Mikić, Z., and Lee, M.: 2006, *Space Sci. Rev.,* this volume*,* doi: 10.1007/s11214-006-9012-2.
Moon, Y.-J., Chae, J., Choe, G. S., Wang, H., Park, Y. D., Yun, H. S., *et al.*: 2002, *Astrophys. J.* **574**, 1066–1073.
Moon, Y.-J., Choe, G. S., Wang, H., and Park, Y. D.: 2003, *Astrophys. J.* **588**, 1176–1182.
Munro, R. H., Gosling, J. T., Hildner, E., MacQueen, R. M., Poland, A. I., and Ross, C. L.: 1979, *Sol. Phys.* **61**, 201–215.
Nindos, A., and Zhang, H.: 2002, *Astrophys. J.* **573**, L133–L136.
Nitta, N. V., and Hudson, H. S.: 2001, *Geophys. Res. Lett.* **28**, 3801–3804.
November, L. J., and Simon, G. W.: 1988, *Astrophys. J.* **333**, 427–442.
Pevtsov, A. A., and Canfield, R. C.: 1999, *Measurement Techniques in Space Plasmas Fields*, pp. 103.
Pick, M., Forbes, T. G., Mann, G., *et al.*: 2006, *Space Sci. Rev.*, this volume doi: 10.1007/s11214-006-9021-1.
Plunkett, S. P., Michels, D. J., Howard, R. A., Brueckner, G. E., St. Cyr, O. C., Thompson, B. J., *et al.*: 2002, *Adv. Space Res.* **29**, 1473–1488.
Plunkett, S. P., Thompson, B. J., Howard, R. A., Michels, D. J., St. Cyr, O. C., Tappin, S. J., *et al.*: 1998, *Geophys. Res. Lett.* **25**, 2477–2480.
Plunkett, S. P., Vourlidas, A., Šimberová, S., Karlický, M., Kotrč, P., Heinzel, P., *et al.*: 2000, *Sol. Phys.* **194**, 371–391.
Poland, A. I., and MacQueen, R. M.: 1981, *Sol. Phys.* **71**, 361–379.
Priest, E. R.: 1984, *Solar magneto-hydrodynamics*. Geophysics and Astrophysics Monographs, Reidel, Dordrecht, 1984.
Priest, E. R., Gaizauskas, V., Hagyard, M. H., Schmahl, E. J., and Webb, D. F.: 1986, *Energetic Phenomena on the Sun*, pp. 1–1.
Roussev, I. I., Sokolov, I. V., Forbes, T. G., Gombosi, T. I., Lee, M. A., and Sakai, J. I.: 2004a, *Astrophys. J.* **605**, L73–L76.
Roussev, I. I., Sokolov, I. V., Forbes, T. G., Gombosi, T. I., Lee, M. A., and Sakai, J. I.: 2004b, *Astrophys. J.* **605**, L73–L76.

Rust, D. M., and Kumar, A.: 1994a, *Sol. Phys.* **155**, 69–97.
Rust, D. M., and Kumar, A.: 1994b, *ESA SP-373: Solar Dynamic Phenomena and Solar Wind Consequences, the Third SOHO Workshop*, pp. 39.
Rust, D. M., and Kumar, A.: 1996, *Astrophys. J.* **464**, L199–L202.
Saito, K., and Tandberg-Hanssen, E.: 1973, *Sol. Phys.* **31**, 105–121.
Sheeley, N. R., Walters, J. H., Wang, Y.-M., and Howard, R. A.: 1999, *J. Geophys. Res.* **104**, 24739–24768.
Simnett, G. M.: 1999, *The Many Faces of the Sun: A Summary of The Results from NASA's Solar Maximum Mission*, pp. 201.
Srivastava, N., Schwenn, R., and Stenborg, G.: 1999, *ESA SP-446: 8th SOHO Workshop: Plasma Dynamics and Diagnostics in the Solar Transition Region and Corona*, pp. 621.
St. Cyr, O. C., Burkepile, J. T., Hundhausen, A. J., and Lecinski, A. R.: 1999, *J. Geophys. Res.* **104**, 12493–12506.
Sterling, A. C., Hudson, H. S., Thompson, B. J., and Zarro, D. M.: 2000, *Astrophys. J.* **532**, 628–647.
Sterling, A. C., and Moore, R. L.: 2001a, *Astrophys. J.* **560**, 1045–1057.
Sterling, A. C., and Moore, R. L.: 2001b, *J. Geophys. Res.* **106**, 25227–25238.
Subramanian, P., and Dere, K. P.: 2001, *Astrophys. J.* **561**, 372–395.
Tandberg-Hanssen, E.: 1995, *The Nature of Solar Prominences*. Astrophysics and Space Science Library, vol. 199, Kluwer Academic Publishers, Dordrecht, c1995.
Tappin, S. J., and Simnett, G. M.: 1997, *ESA SP-415: Correlated Phenomena at the Sun, in the Heliosphere and in Geospace*, pp. 117–120.
Thompson, B. J., Plunkett, S. P., Gurman, J. B., Newmark, J. S., St. Cyr, O. C., and Michels, D. J.: 1998, *Geophys. Res. Lett.* **25**, 2465–2468.
Tripathi, D., Bothmer, V., and Cremades, H.: 2004, *A&A* **422**, 337–349.
Vaiana, G. S., Krieger, A. S., and Timothy, A. F.: 1973, *Sol. Phys.* **32**, 81–116.
van Ballegooijen, A. A., Priest, E. R., and Mackay, D. H.: 2000, *Astrophys. J.* **539**, 983–994.
Vourlidas, A., Buzasi, D., Howard, R. A., and Esfandiari, E.: 2002, *ESA SP-506: Solar Variability: From Core to Outer Frontiers*, pp. 91–94.
Wang, H.: 1993, *ASP Conf. Ser. 46: IAU Colloq. 141: The Magnetic and Velocity Fields of Solar Active Regions*, pp. 323–332.
Wang, Y.-M., and Sheeley, N. R.: 1999, *Astrophys. J.* **510**, L157–L160.
Wang, Y.-M., and Sheeley, N. R.: 2002, *Astrophys. J.* **575**, 542–552.
Wang, Y.-M., Sheeley, N. R., Socker, D. G., Howard, R. A., Brueckner, G. E., Michels, D. J., *et al.*: 1998, *Astrophys. J.* **508**, 899–907.
Webb, D. F., Krieger, A. S., and Rust, D. M.: 1976, *Sol. Phys.* **48**, 159–186.
Webb, D. F., Lepping, R. P., Burlaga, L. F., DeForest, C. E., Larson, D. E., Martin, S. F., *et al.*: 2000, *J. Geophys. Res.* **105**, 27251–27260.
Webb, D. F., Nolte, J. T., Solodyna, C. V., and McIntosh, P. S.: 1978, *Sol. Phys.* **58**, 389–396.
Welsch, B. T., DeVore, C. R., and Antiochos, S. K.: 2005, *Astrophys. J.* **634**, 1395–1404.
Welsch, B. T., Fisher, G. H., Abbett, W. P., and Regnier, S.: 2004, *Astrophys. J.* **610**, 1148–1156.
Wills-Davey, M. J., and Thompson, B. J.: 1999, *Sol. Phys.* **190**, 467–483.
Wolfson, R., Conover, C., and Illing, R. M. E.: 1987, *BASS* **19**, 931.
Wolfson, R., and Saran, S.: 1998, *Astrophys. J.* **499**, 496–503.
Wood, B. E., Karovska, M., Chen, J., Brueckner, G. E., Cook, J. W., and Howard, R. A.: 1999, *Astrophys. J.* **512**, 484–495.
Yang, G., and Wang, H.: 2002, *Solar-Terrestrial Magnetic Activity and Space Environment*, pp. 113–116.
Zarro, D. M., Sterling, A. C., Thompson, B. J., Hudson, H. S., and Nitta, N.: 1999, *Astrophys. J.* **520**, L139–L142.
Zwaan, C.: 1985, *Sol. Phys.* **100**, 397–414.